J MATER SCI 41 (2006) 793–815

Nanomagnetism and spin electronics: materials, microstructure and novel properties

K. M. KRISHNAN*, A. B. PAKHOMOV, Y. BAO, P. BLOMQVIST, Y. CHUN, M. GONZALES, K. GRIFFIN, X. JI, B. K. ROBERTS
Department of Materials Science and Engineering, University of Washington, Box 352120, Seattle, WA, 98195-2120
E-mail: kannanmk@u.washington.edu

We present an overview of the critical issues of current interest in magnetic and magnetoelectronic materials. A broad demonstration of the successful blend of materials synthesis, microstructural evolution and control, new physics and novel applications that is central to research in this field is presented. The critical role of size, especially at the nanometer length scale, dimensionality, as it pertains to thin films and interfaces, and the overall microstructure, in determining a range of fundamental properties and potential applications, is emphasized. Even though the article is broad in scope, examples are drawn mainly from our recent work in magnetic nanoparticles and core-shell structures, exchange, proximity and interface effects in thin film heterostructures, and dilute magnetic dielectrics, a new class of materials for spin electronics applications.

1. Introduction

Magnetism, subtle in its manifestations, is electronically driven but weak compared with electrostatic interactions. It has its origin in quantum mechanics, i.e. the Pauli exclusion principle and the existence of electron spin. However, it is also known for a variety of classical effects, arising from both short- and long-range forces and is widely associated with "microstructure" or the morphological arrangements of phases, grains or individual atoms themselves. These are, in part, the reasons for the richness of structures and properties encountered in magnetic systems from which various useful and technological applications arise [1]. These are also, in part, the reasons why the collective magnetic behavior of materials is complex, poorly understood and many fundamental questions remain unanswered.

There are clearly two limits to magnetic behavior as a function of size and dimensionality. At one end of the spectrum (bulk) the microstructure determines the magnetic (hard and soft) behavior. It is a function of the processing method and our understanding of it is qualitative and empirical at best. At the other end, as the length scales approach the size of domain wall-widths (nanostructures), lateral confinement (shape and size) and inter-particle exchange effects dominate, rendering classical descriptions grossly inadequate, until finally, at atomic dimensions quantum-mechanical tunneling effects are expected to predominate [2].

In the ideal case, considering only dipolar interactions, the spin-flip barrier for a small magnetic object [3] is a product of the square of the saturation magnetization, M_s and its volume ($V \sim a^3$). As a first approximation, one can set this equal to the thermal energy, i.e. $M_s{}^2\ a^3 \sim k_B T \sim 25$ meV at room temperature, and for typical ferromagnets obtain a characteristic length $a \sim 4$ nm, below which they do not behave as ferromagnets any more. In practice, changes in magnetization of a material occur via activation over an energy barrier and associated with each type of energy barrier is a different physical mechanism and a characteristic length. These fundamental lengths are the crystalline anisotropy length ($l_K \sim (J/K)$, the magnetostatic length ($l_s \sim \sqrt{J/(2\pi \cdot M_s{}^2)}$) and the applied field length ($l_H \sim (2J/H \cdot M_s)$. Here J is the interatomic exchange, K is the anisotropy constant of the bulk materials and H the applied field. In principle, if multiple barriers are present, for a given time, the one with the shortest characteristic length determines the materials properties [4]. For a general anisotropy, K, a characteristic time, τ, for reversal is determined as $\tau \sim \tau_0 \exp(K \cdot V/k_B T)$. If the measurement time (typically 100 s) is included, one can then determine a characteristic size (V_{sp}) at room temperature or, for a given volume, a characteristic

*Author to whom all correspondence should be addressed.
0022-2461
DOI: 10.1007/s10853-006-6564-1

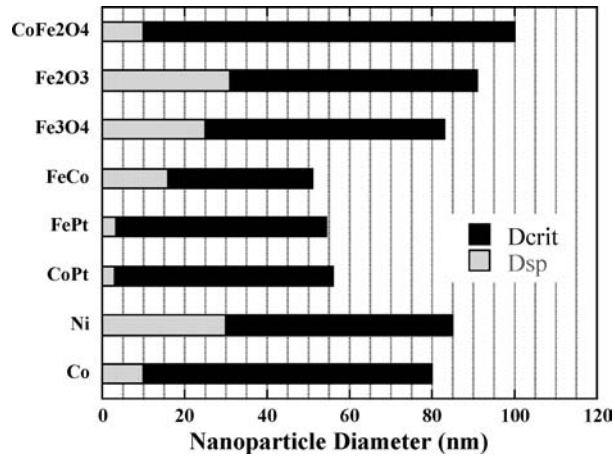

Figure 1 Single domain size, D_{crit} and magnetic stability size or the superparamagnetic limit at room temperature, D_{sp} for some common ferromagnetic materials.

temperature called the blocking temperature, T_b that defines a transition from ferromagnetic to a thermally unstable or superparamagnetic behavior. Further, if the particle sizes become larger, instead of being uniformly magnetized (single domain), the particles can break into multiple domains to minimize their overall energy. Using theories for domain stability in fine particles [5] and bulk properties available in the literature, one can determine the characteristic size up to which single domains are stable. This series of magnetic "phases" as a function of size is shown (Fig. 1) for different ferromagnets and includes a "single domain" size (D_{crit}) below which the material will not support a multi-domain particle [6] and a size (D_{sp}) defined by the super-paramagnetic effect [7] below which a spontaneous flip in magnetization occurs due to thermal effects at room temperature.

Such nanostructures in the size range identified in Fig. 1, which can be considered to be zero-dimensional objects, can be made by three distinct approaches – metallurgy, chemical synthesis and lithography (Fig. 2). The metallurgical approach involves the synthesis of alloys by rapid solidification that on subsequent annealing phase segregates with a microstructure on the nanometer length scale. Such an approach is used for preparing very soft [8] commercial magnets or very hard [9] magnets. The former is achieved by creating nanoscale crystallites that are randomly oriented but interact strongly to give a very small effective anisotropy by directional averaging. On the other hand, large anisotropies and coercivities very close to the theoretical maximum can be obtained by creating isolated magnetic particles in a non-magnetic matrix [10, 11]. The alternative, well-known method to create nanoscale objects is by lithography. This top-down approach, carried out with either electrons or photons, is both time consuming and expensive but recent variations also include locally patterning a specific property, such as the magnetic anisotropy, by implantation through a stencil

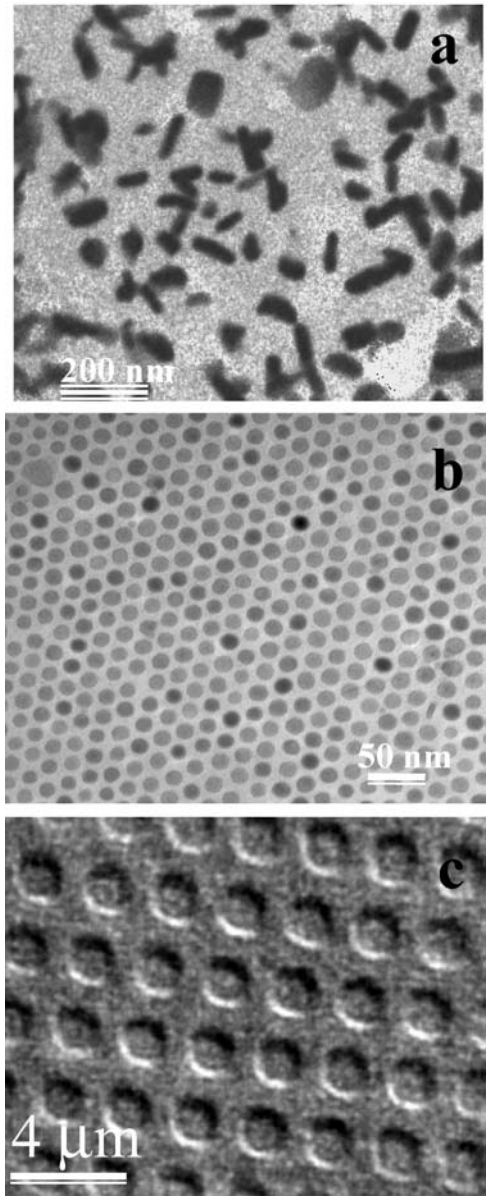

Figure 2 Alternative routes for the fabrication of zero-dimensional structures. (a) Metallurgical—Hard $Nd_2Fe_{14}B$ precipitates in a non-magnetic Nd matrix [10]; (b) Chemical—10 nm dia cobalt nanoparticles synthesized by chemical routes and self-assembled on a TEM carbon grid and (c) Lithography—arrays formed by ion-implantation through stencil masks—a top down approach [12].

mask [12]. The third approach is to chemically synthesize nanoparticles by the rapid decomposition of a metalorganic precursor by injecting it in a coordinating solvent containing surfactants at elevated temperature [13, 14]. Details of our work using the last method, including the synthesis of core-shell particles, their magnetic behavior and self-assembly, as well as their potential in biomedical applications are discussed later in this article.

The effect of dimensionality on magnetic behavior is best studied in thin film heterostructures. Their

magnetic behavior is rich in new phenomena and includes recent highlights such as surface/interface anisotropy that leads to perpendicular anisotropy in multilayer structures [15] as well as frustration, proximity and interface effects that lead to exchange bias (ferromagnetic/antiferromagnetic bilayers) [16] and exchange spring (ferromagnetic/ferromagnetic bilayers) [17] behavior. These magnetic properties are dominated by the physical, chemical and magnetic structure of their interfaces and it is important that appropriate tools be developed for studying them most effectively at relevant length scales [18, 19].

The basic energies involved in the manipulation and control of the magnetic properties of thin film heterostructures are exchange (controls magnetic order) and anisotropy (controls magnetic orientation). These are phenomenological descriptions of fundamental correlations and energies arising from the electronic and crystalline structure of the material [20]. A soft ferromagnet (FM) such as iron has a large exchange parameter but a small anisotropy, making ferromagnetic order stable at higher temperatures but with unpredictable orientation of magnetization, especially if it is of nanoscale dimension. On the other hand, many antiferromagnets (AFM) have large anisotropies and consequently, very stable orientations. In FM-AFM heterostructures, exchange coupling between these layers can produce a ferromagnet with stable order and high anisotropy, with the latter having unidirectional character—an unusual feature not observed in ferromagnets. This phenomenon is called exchange bias (EB) because the hysteresis loop is shifted and centered on a non-zero magnetic field. In spite of the simple physics, in reality EB films show a variety of unusual behavior that includes enhanced coercivity [21], magnetic training effects [22], perpendicular coupling [23], kinked hysteresis loops [24] and an asymmetry in the magnetization reversal process [25]. A number of theoretical models proposed [26] have provided varying insight into the exchange bias phenomenon but none of them have been able to provide a comprehensive description of all its salient features. Our recent work [27], involving epitaxial growth of high quality thin films, structural characterization by X-ray diffraction, neutron reflectivity and domain imaging using synchrotron radiation has shown that there is a fundamental *asymmetry* in the reversal mechanism of such structures. On one branch of the hysteresis reversal takes place by domain nucleation whilst, in the other direction, it occurs by domain wall rotation.

For a ferromagnetic thin film or multilayer the anisotropy energy, E_{an} is written in terms of an effective anisotropy constant, K_{eff} as $E_{an} \sim K_{eff} \sin^2\theta$. K_{eff} includes contributions from the demagnetizing field or shape anisotropy, surface/interface anisotropy and volume magnetocrystalline anisotropy. For thick films (t_M>few nm for transition metals), the shape anisotropy energy contribution is predominant and the magnetization lies in the plane of the film. For ultrathin films and multilayers (t_M<$\sim$1 nm), it has been suggested that the surface/interface anisotropy contribution, arising from a break in symmetry at the interface [28] and proportional to t_M^{-1}, can overcome the shape anisotropy and result in a spontaneous magnetization perpendicular to the film. Such perpendicular anisotropy in multilayers is now well known [15] but, in practice, an understanding of the origin of this phenomenon requires a careful evaluation of the evolution and control of their complex microstructure at the atomic scale [29]. Recently, we have combined these two phenomena, i.e. perpendicular anisotropy and exchange bias and critically evaluated the role of interfaces in such perpendicularly exchange-biased systems. Details of our work in such thin film structures is also discussed later.

Part of the interest in magnetic anisotropy and exchange bias in thin films and multilayers is related to the practically important area of spintronics, or spin electronics [30]. Spintronics is an inter-disciplinary field of research which includes the studies of electronic materials/devices that explicitly employ the spin degree of freedom of the current carriers. Recent successful developments include giant magnetoresistance (GMR) in magnetic metal multilayers [31], spin valve devices [32], and tunneling magnetoresistance (TMR) in magnetic tunnel junctions [33], that are intended primarily for applications in magnetic field-sensing elements such as read heads and non-volatile magnetic random access memories (MRAMs). Spin valve heads are already used in industry; MRAM prototype structures have been demonstrated [34]. Spin manipulation in semiconductors is an attractive alternative for applications in the future generations of sensors, memory, logic, and possibly quantum computing architectures. Many spintronic designs include electrical injection and sensing of magnetic moment associated with the spin of the charge carrier. However, spin injection from a ferromagnetic metal electrode attached to a semiconductor structure is very inefficient due to several reasons including simple impedance mismatch which is shown to lead to spin loss [35]. It has been proposed that a *ferromagnetic semiconductor* with highly (ideally 100%) spin-polarized carriers can be effectively used for this application. Recent interest in ferromagnetic semiconductors, in particular the so-called "dilute magnetic semiconductors" (DMS) [36, 37], is justified both by their potential use as spin-injecting materials and the new physics describing the properties of these materials. The best-studied DMS material so far, Mn-doped GaAs, was discovered in 1996, but is not likely to find practical applications because of the low Curie temperature of $\sim$170 K. Our fundamental studies are directed at understanding the nature of ferromagnetism in wide band gap DMS with the Curie temperatures above room tempera-

ture. In this article, we will briefly describe some of our recent work in this area. In particular, careful synthesis and detailed magnetic/transport measurements, complemented by advanced characterization of doped transition metal oxides has led to the discovery of a new class of spintronics materials – "dilute magnetic dielectrics" or DMD [38]. These results also lead us to propose different operating principles for spintronic devices.

Finally, the optimization and understanding of the magnetic and transport properties of this range of materials, be they nanoparticles or thin film heterostructures, requires a dynamic iteration between synthesis, property measurements and the evaluation/control of microstructure (physical, chemical & magnetic) at the appropriate length scales [39]. There are three length scales that are relevant: the *characteristic length* associated with the dimensional characteristics of the magnetic phenomenon of interest, the *size* of the microstructural features arising from the processing and the *interaction length* of the probe being used to characterize these materials. It is important to identify the range where these three length scales overlap, for it is there that not only novel properties and phenomenon are usually observed but a meaningful interpretation of the role of microstructure can be made. For materials of interest in nanomagnetism and spin electronics these length scales can range from the atomic (interfaces) to a few tens of nanometers (grain sizes). Hence, in addition to synthesis/processing, advances in the development of such materials will critically depend on our ability to characterize them by a range of electron-optic and X-ray scattering/dichroism techniques. These include transmission electron microscopy [39], electron energy loss spectroscopy with focused probes and the related energy-filtered imaging methods [40, 41]; magnetic spectroscopy [42] or imaging either in transmission [43] or photoemission [44] using synchrotron radiation and utilizing circular dichroism for magnetic contrast.

In the context of the above, we will present details of our work in three distinct areas: magnetic nanoparticles, thin film heterostructures, and doped magnetic oxide thin films.

2. Magnetic nanoparticles and core-shell structures

2.1. Synthesis

Magnetic nanoparticles have drawn much attention recently due to their potential in magnetic recording as well as many biological and medical applications such as magnetic separation, hyperthermia treatment, magnetic resonance contrast enhancement and drug delivery [45]. Synthesis of magnetic nanoparticles with controlled size, shape, composition, morphology, and surface chemistry is of great importance since their magnetic properties are not only affected by all these factors, but they also need to be specifically tuned depending on the requirements of a particular application. Using cobalt as a model system [46, 47], we systematically studied the nucleation and growth of nanoparticles under various thermodynamic/kinetic conditions and developed a general methodology to fabricate a variety of magnetic nanoparticles with desirable morphologies and controlled magnetic properties. Cobalt nanocrystals are obtained by the rapid thermal decomposition of cobalt carbonyl in a surfactant mixture, forming the metal nanoparticle core and soft organic shell. The synthesis initially follows the classic La Mer mechanism [48] (short-burst nucleation and slow growth); however, further particle growth is strongly dependent on the available monomer concentration and the existing surfactants in the system, which can result in different morphologies of nanoparticles. The structure and properties of the surfactants play an important role in the morphology, shape control—because the surfactants affect the reactivity of the monomers and the nuclei concentration—and long term stability of the nanoparticles [49]. Our experimental results show that single crystal cobalt nanocrystals are obtained when oleic acid (OA)/trioctylphosphine oxide (TOPO) are used; however, using the oleic acid (OA)/dioctylamine (DOA) surfactant pair will give rise to multiple grain morphology. In addition, disc-shape particles can be produced when oleic acid (OA) and oleylamine (ON) are present in the synthesis.

By adjusting the ratio of the concentration of surfactants to precursor and the relative bonding strength of the surfactants, we synthesize spherical cobalt nanocrystals with narrow size distribution in the size range of 5–25 nm, and anisotropic cobalt nanodiscs with specific aspect ratios. Anisotropic cobalt nanoparticles are obtained by rapid growth in a surfactant mixture under kinetic conditions, where the different surfactants are used to selectively control the growth rates of the different crystal faces. Two typical examples of cobalt nanocrystals with different morphologies are shown is Fig. 3. Here, cobalt nanodiscs appear like "nanorods" in TEM images, due to the strong hydrophobic interaction between surfactant tails, which tends to draw them together. Therefore, disks will stack face to face in order to maximize contact between surfactant tails, and thus minimizing exposure to air. The magnetostatic energy is also a minimum when the neighboring disks lie face to face.

2.2. Self-assembly of cobalt nanocrystals

Self-assembly is the spontaneous organization of molecules, molecular clusters or nanoscale objects into 2D arrays and/or 3D networks by weak interactions. For magnetic nanoparticles, in addition to the van der Waals attraction between metallic cores and the repulsive forces from the surfactant chains, magnetic interaction will also play a critical role. Using cobalt nanocrystals as building

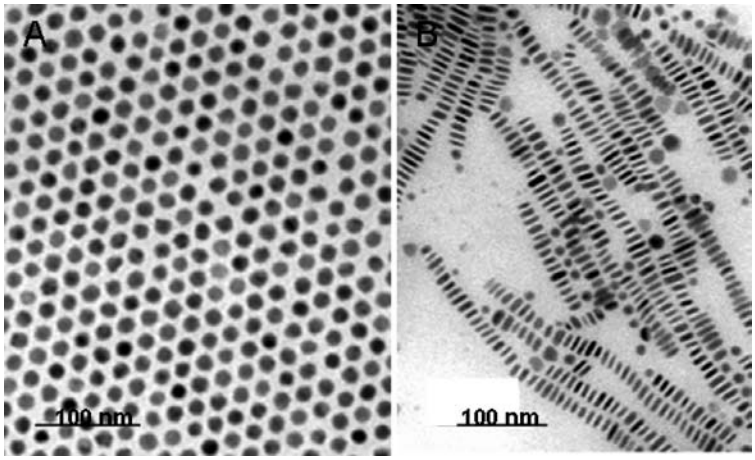

Figure 3 Two examples of cobalt nanocrystals (A) 10 nm nanospheres and (B) 5×20 nm anisotropic nanodiscs.

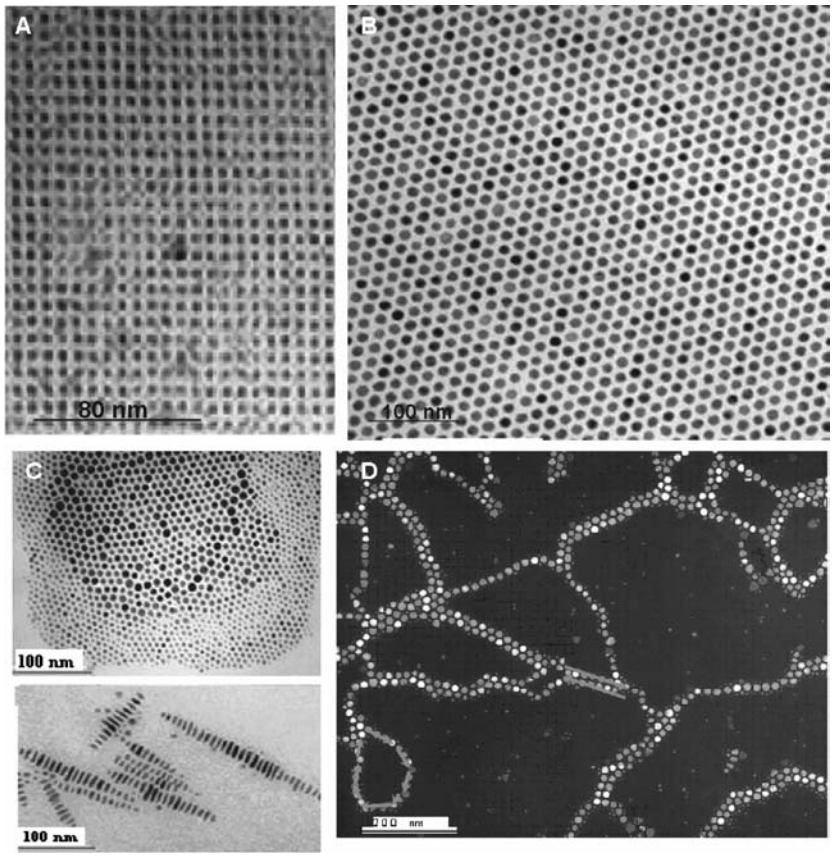

Figure 4 Self-assembly behavior of Cobalt nanocrystals as a function of particle size, (A) square packing for 4 nm nanoparticles, (B) hexagonal closed packing for 8–10 nm nanoparticles, (C) Bimodal distribution of two different size particles and (D) linear chains for 18 nm larger nanoparticles.

blocks, we systematically studied the self-assembly behavior of these nanocrystals as a function of particle size and shape. Depending on particle size and shape, one of the set of competing weak forces (steric, van der Waals, entropy and magnetostatic) will dominate the self-assembly and determine the resulting organization. In this fashion, we are able to selectively achieve square packing, hexagonal close packing, linear chains and for bimodal size distributions of cobalt nanospheres spatial segregation as a function of particle size [50] (Fig. 4). A square arrangement is observed for small size nanoparticles to minimize the repulsive steric forces between the surfactant molecules on their surface. The interaction of surfactant chain significantly affects the organization behavior of these nanoparticles, since almost 50% of the atoms are on the surface and are bonded to the surfactants

when particle size is smaller than 5 nm. As particle size increases, the surface atoms become less and less dominating. The nanoparticles behave like hard-spheres and self-assemble in a 2D hexagonal arrangement resulting from a first order phase transition as a function of concentration. On the other hand, if these two sizes are combined to give a bimodal-size distribution the vibrational entropy of the system dominates. This leads to a preferential wetting of the surface by the larger particles such that the larger size particles are located in the center and are surrounded by the smaller size nanoparticles. Such "fictitious" forces arising from the entropy of the system, called the depletion force, have been proposed in theoretical discussion of soft materials [51]. Cobalt nanocrystals become ferromagnetic when particle diameter is larger than 10 nm. Hence, as the particle size increases, the magnetostatic interaction become significant, and linear chains or loops are formed. For anisotropic nanodiscs, lyotropic liquid-crystal-like arrays with increased orientation order as a function of concentration are observed in the TEM image (Fig. 5).

2.3. Core-shell nanocrystals

The strategies developed for the synthesis of nanoparticles in homogenous solution can be extended to the general case by separating the particle nucleation from its subsequent growth stage. When the nuclei are different from available monomer materials, particles composed of binary elements can be easily synthesized if conditions suitable for heterogeneous nucleation can be generated in solution. The final morphology of such binary particles is dependent on their bulk thermodynamics: for immiscible heterogeneous systems core-shell structures are obtained whilst miscible systems lead to alloy nanoparticles. Here we are particularly interested in the core-shell structures, since the biological applications of cobalt NPs are limited by their poor biocompatibility and resistance to oxidation. It would be ideal if the shell could provide stability, biocompatibility and additional functionality. Most importantly, the shell materials should be immiscible with the core materials. Considering all these requirements, gold becomes a natural choice for the shell material.

Gold coated magnetic nanoparticles have been reported by different groups [52–54] However, in addition to reproducibility, the growth processes do not lend themselves to the production of uniformly coated core-shell particles because the synthesis environment is rich in oxygen and the presence of water accelerates the formation of cobalt hydroxide. Moreover, in this method, the use of a strong reducing agent (borohydride) makes the reduction reaction too rapid to form a uniform shell. It is also possible that instead of forming a shell, individual Au nanoparticles are formed.

Using pre-made cobalt nanoparticles as seeds, we grow a gold shell in solution by slowly reducing a low-reactivity gold precursor with a weak reducer under mild conditions (85–105°C) to form $Co_{core}Au_{shell}$ nanoparticles. Subsequently, these core-shell nanoparticles are made water-soluble by functionalizing them with hydrophilic thiol-containing surfactants, 11-mercaptoundecanoic acid, through the specific binding between gold and thiols. These $Co_{core}Au_{shell}$ nanoparticles have been extensively characterized by a wide range of transmission electron microscopy methods. The contrast of the particles in routine transmission electron microscopy (TEM) images—lighter core and the darker shell—suggests the core-shell structure is formed (Fig. 6A). High resolution TEM image show a single crystal Co core uniformly surrounded by multiple gold grains, suggesting that gold has multiple nucleation sites on cobalt seeds during synthesis (Fig. 6B). The image clearly shows the structure of the shell, but the

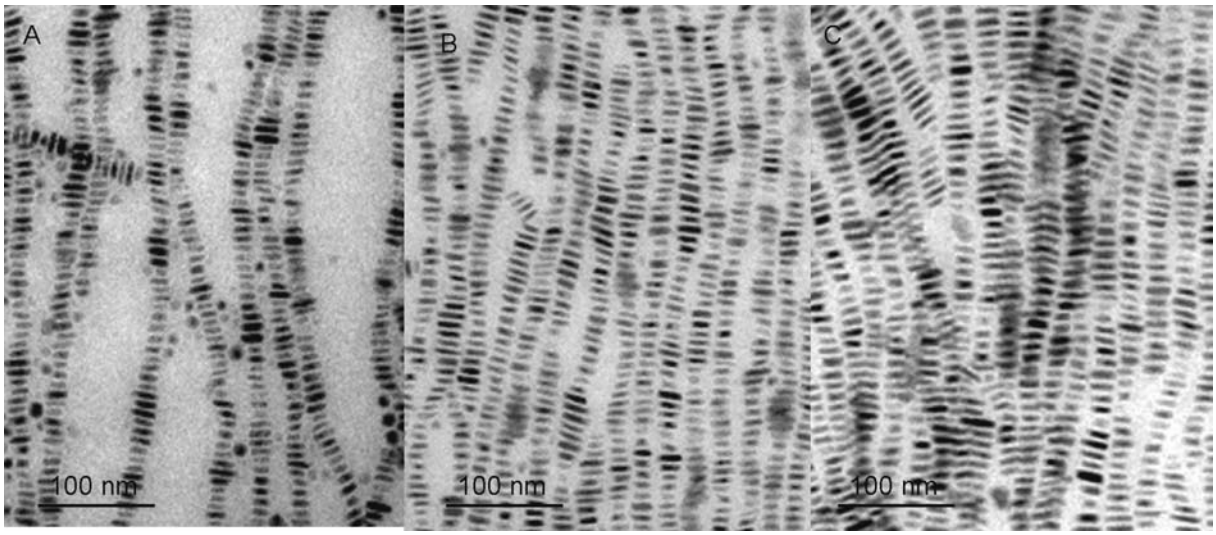

Figure 5 Lyotropic liquid crystal behavior of cobalt naodiscs and show an increase in orientational order with increasing concentration (A, B, C).

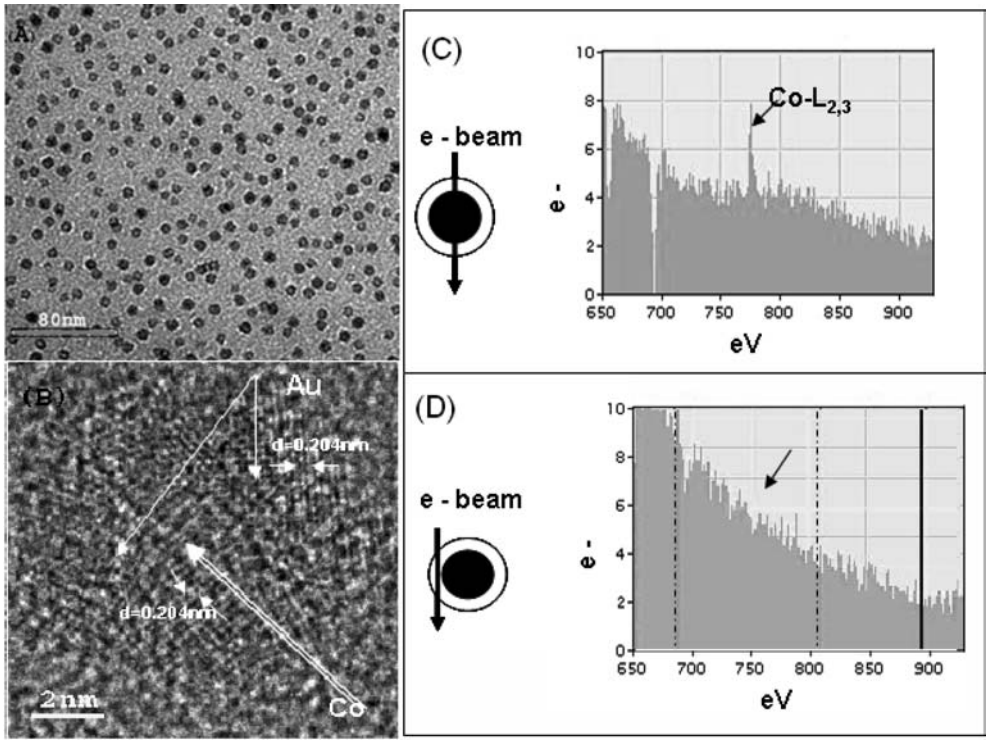

Figure 6 (A) 9 nm $Co_{core}Au_{shell}$ nanoparticles: bright field TEM image, (B) high resolution TEM image, (C) EELS spectra of $Co_{core}Au_{shell}$ nanoparticles from center and (D) EELS spectra of $Co_{core}Au_{shell}$ nanoparticles edge.

core is not well-resolved due to it being both in a different crystallographic orientation and embedded inside the thin shell. Lattice spacing of 0.204 nm and 0.102 nm, directly measured from the image, corresponds to fcc Au (002) and (004) planes. An inverse Fourier transform analysis was performed on separate images from different regions of the Au shell, and the projected symmetry of local images fits well to fcc Au structure as well. The observation of Co-$L_{2,3}$ edges in electron energy-loss spectroscopy using a 1 nm probe focused on the core, (and absence of the peak when focused on the shell) confirms the distinct chemical nature of the core (Co) and shell (Au) (Fig. 6C and D).

Complementing this detailed TEM analysis, bulk structural and magnetic properties of these nanoparticles were investigated on powder form samples by X-ray diffraction (XRD) and superconducting quantum interference device (SQUID) magnetometry, and the optical properties in solution form by UV-Visible spectrophotometery. The relatively sharp peak of this core-shell structure in $\theta - 2\theta$ X-ray scans demonstrates a reasonably high degree of crystallinity and uniform particle size of these core-shell nanoparticles (Fig. 7A). The temperature dependent magnetization measurements show a narrow peak at 55 K, suggesting the magnetic size of the particle is about 6 nm with a narrow size distribution by comparing with pure cobalt nanoparticle measurement (Fig. 7B). At lower temperatures (5 K) the nanoparticles show hysteresis behavior consistent with the ferromagnetic state (Fig. 7B, inset).

In addition to the intrinsic magnetic properties of the cobalt core, the gold nanoshell brings in unique biocompatibility and near infrared optical activity. The plasmon-derived optical resonance of the gold shell can be dramatically shifted in wavelength from the visible region into infrared over a wavelength range that spans the region of highest physiological transmissivity. From UV-visible spectra, pure Co nanoparticles show a continuous increase in intensity with decreasing wavelength and no peak is observed; pure Au nanoparticles show a characteristic peak around 530 nm; however, a relatively strong peak at 680 nm was observed for the Au shell absorbance of these Co-Au core-shell nanoparticles (Fig. 7C). This red shift from 530 nm to 680 nm compared to similar size individual gold nanoparticles also suggests the existence of the core-shell structures.

2.4. Biomedical applications of magnetic nanoparticles: diagnostics and therapeutics

The use of nanoparticles in biological applications is attractive because their small size allows them to interact with biological molecules and systems in ways not previously possible with larger objects. Nanoparticles made from magnetic materials have an added level of functionality. Their magnetic properties open up the potential for novel treatments utilizing magnetic phenomena as well as non-invasive and targeted therapy methods and

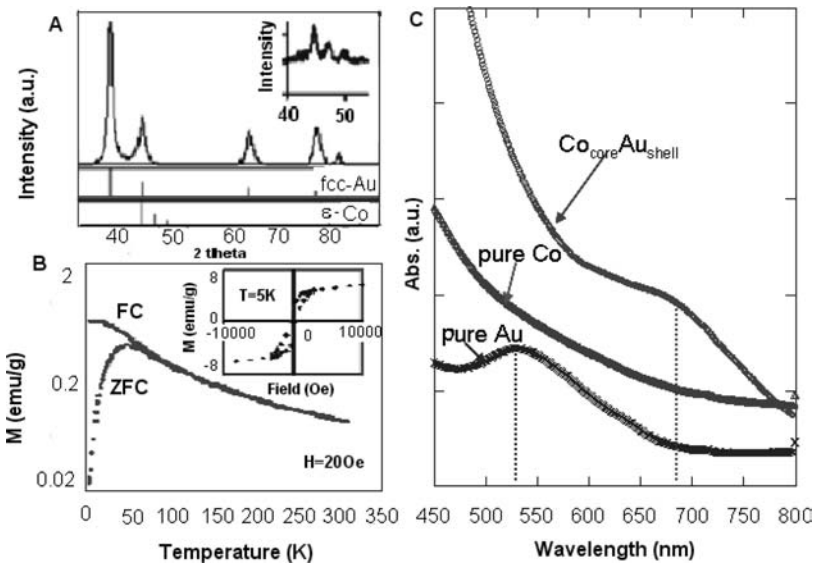

Figure 7 $Co_{core}Au_{shell}$ nanoparticles, (A) $\theta \sim 2\theta$ X-ray scan. Inset is pure ε-Co spectrum, (B) ZFC/FC magnetic measurements, inset 5K hysteresis and (C) UV-visible spectra and the comparison with pure cobalt and gold nanoparticles.

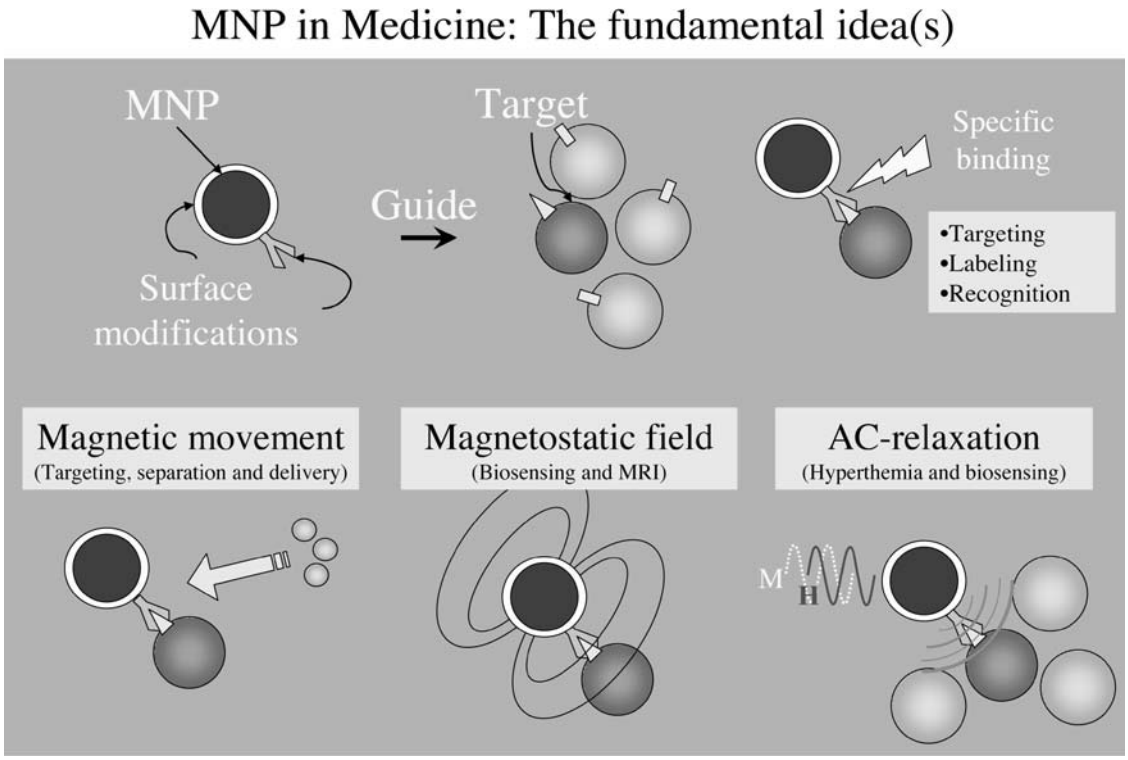

Figure 8 Prior to use in bioapplications the surface of magnetic nanoparticles must be modified to provide functionality (specific binding is ideal). After localization at the target the magnetic properties of the particles provides novel functionality. Moving the particles with magnetic field gradients allows for magnetic targeting, separations and delivery. The particle's magnetostatic field allows for diagnostics *in vitro* (microfluidics based biosensing) and *in vivo* (MRI contrast enhancement). The dynamic relaxation of the particles can be used for therapeutics (hyperthermia) or diagnostics (biosensing).

diagnostics (Fig. 8). For bioapplications there are three parameters that will determine the performance of magnetic nanoparticles: the surface chemistry, size (magnetic core, hydrodynamic volume and size distribution) and the magnetic properties of the particles. The surface chemistry and size will control the interaction of the particles with biomolecules by providing biocompatibility, targeting, controlled circulation time and specific binding. The physical and chemical properties of the particles themselves, i.e. the size, size distribution, shape, crystallinity

and composition, will control the magnetic properties and response of the particles to magnetic fields. Our work is rooted in our ability to control the morphology of the particles as well as tailor their magnetic properties for specific applications.

Movement of magnetic particles with a magnetic field gradient can be used to isolate, move or deliver biological molecules or cells. Biomolecules of interest can be concentrated in or separated from solutions via specific binding to complementary biomolecules coated on the surface of magnetic nanoparticles. Drugs can be delivered locally when they are attached to the surfaces of the particles [55]. The particles can be concentrated at the target location either by specific binding to the target or by localizing the particles magnetically. For this application magnetic forces must be strong enough to overcome viscous drag. Currently, micron size clusters of superparamagnetic iron oxide particles, such as Dynabeads, are commercially available for separations. For applications which require smaller particles, nanoparticles must be made from materials with high moments such as cobalt or iron-platinum [56]. The magnetic fields generated by the particles can be used for diagnostics either *in vivo* or *in vitro*. *In vivo* the magnetic fields generated by the particles can affect the relaxation of protons of surrounding molecules thus providing contrast in MRI [57]. Companies such as Advanced Magnetics have iron oxide nanoparticles commercially available with FDA approval for use as MRI contrast enhancers. *In vitro* magnetic nanoparticles can be bound to a surface via specific binding between biomolecules of interest and their compliments attached to the surface of the nanoparticles. This binding event can be detected with a GMR [58] or planar Hall sensor [59] and used to identify unknown biomolecules.

The relaxation of magnetic nanoparticles in an AC magnetic field can be used for both diagnostics and therapeutics. Blocked particles relax via Brownian relaxation, with a relaxation time, τ_B given by $\tau_B = 3\eta V_H/k_B T$, where η is the viscosity of the matrix and V_H is the hydrodynamic volume of the particle (particle core plus surface coating and any associated layer). Brownian relaxation is dependent on the ability of the particles to rotate in their matrix, thus changes in the viscosity [60] or the hydrodynamic radius [61] can be detected by measuring the shift in frequency at which there is a peak in the imaginary component of the susceptibility. In this sense the nanoparticles can be used as a biosensor to detect binding events of biomolecules of interest on the surface of the functionalized particles. On the other hand, small unblocked particles relax via Néel relaxation, a rotation of the magnetic moment with an associated time constant, $\tau_N = \sqrt{\pi}/2\tau_0 \exp(KV_M/k_B T)/(KV_M/k_B \mathrm{T})^{1/2}$ which is dependent on the magnetic anisotropy of the particles. Such relaxation of magnetic nanoparticles in an AC magnetic field can generate heat where the increase in temperature is dependent on the time, frequency, the amplitude of the magnetic field, the relaxation dynamics and the mechanism of thermal dissipation in the medium. For high heating rates the frequency must be correlated to the relaxation and thus the properties of the magnetic particles. For bioapplications involving heat generation it is preferable to remain in the Néel relaxation regime as it is then possible to generate higher heating rates. Additionally, such heating is easier to model because the relaxation is independent of the surface coatings or mobility of the nanoparticles. Changes in mobility can occur if the particles are located in tissue of varying viscosities (i.e. blood, muscle, fat) or if the particles are free or bound to a cell or protein.

In our work, in addition to metallic/alloy nanoparticles and core-shell structures, we have also prepared highly uniform, monodisperse, single crystal, magnetite Fe_3O_4, nanoparticles of tailorable size (4–11 nm) which we believe are ideal for magnetic fluid hyperthermia. Hyperthermia is the controlled heating of tissue to promote cell necrosis. The use of magnetic nanoparticles in hyperthermia applications has been shown to be a powerful cancer treatment [62, 63]. This method is non-invasive and magnetic fields can be tuned to be invisible to tissue. We are developing methods to understand and predict the dynamic response and heating of the nanoparticles in an ac-magnetic field [64]. After localizing the particles at the target site, ac-magnetic fields will be applied. The frequency and amplitude of the field must be within biologically compatible limits such that $H_o f \leq 4 \times 10^8$ A/ms [65]. The temperature of the target area will increase from 37°C to a target temperature of approximately 42–46°C for approximately 30 min. Combining MRI imaging and drug delivery potential of the magnetic nanoparticles with heating will result in a synergistic cancer treatment.

In order to generate the maximum heat for minimum dosage, it is critical to control the properties of the nanoparticle core and the surface chemistry. The ability of magnetic nanoparticles to generate heat is dependent on particle size (magnetic core and hydrodynamic diameter), crystallinity, shape and particle polydispersity. Predicting the dynamic behavior of ferrofluids in an ac-magnetic field is complex because of coupling between many parameters: the magnetic properties of individual nanoparticles, polydispersity of size and shape, ferrofluid concentration, temperature and viscosity of medium. Most real ferrofluids deviate from ideal behavior due to polydispersity of size and shape and particle interactions. Polydispersity of particle shape can have an effect on the anisotropy constants of the particles whereas particle interaction arising from magnetostatic attraction or particle/solvent interactions can have a large effect on the hydrodynamic radius of the particles. Consequently, polydispersed or agglomerated samples can result in a mixture of relaxation behaviors resulting in lowered heating rates [66] which may be

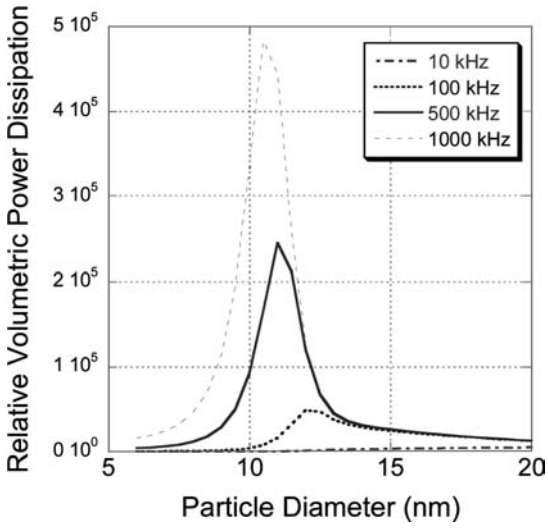

Figure 9 Relative volumetric power dissipation as a function of particle size calculated for our Fe_3O_4 nanoparticles at room temperature in water for 10, 100, 500 and 1000 kHz. The peak near 11 nm is not highly dependent on frequencies and indicates that 11 nm particles will have high heating rates at therapeutic frequencies.

undesirable. Therefore, uniform, non-agglomerated and monodisperse particles, such as ours, are ideal for magnetic fluid hyperthermia. Preliminary models of the relative volumetric power dissipation of our nanoparticles as a function of particle diameter indicate that peak heating will occur for particles around 11 nm for frequencies in the 100 kHz–1 MHz range as shown in Fig. 9. This peak heating occurs for frequencies within a biologically compatible range. By using a technique such as the slit-toroid method [67] the complex susceptibility of ferrofluids is currently being measured. Once the high frequency behavior of our particles is quantified, we will model and study the change in temperature as a function of frequency and field.

3. Thin film heterostructures: Exchange, proximity and interface effects

Advances in the past two decades in the synthesis and characterization of thin film heterostructures and surfaces/interfaces has made it possible to prepare artificially structured materials with tailored magnetic properties [68]. Moreover, magnetism being a cooperative phenomenon, it can be readily manipulated in small structures by the arrangement of different species with varying magnetic interactions that includes proximity, exchange and interface effects. Recent highlights include perpendicular anisotropy observed in metallic multilayers comprised of alternating ferromagnetic layers separated by a nonmagnetic spacer and exchange bias or the observed shift in the hysteresis loop of a ferromagnet grown in close proximity to an antiferromagnet and field-cooled through the Neél temperature. Here we discuss some of our recent work in this area spanning three broad topics: fundamental mechanism of magnetization reversal in exchange biased films, role of interface disorder in both perpendicular anisotropy and exchange bias and the nature of the coupling between ultrathin ferromagnetic-ferromagnetic bilayers.

3.1. Fundamental mechanism of magnetization reversals in exchange biased films

Any systematic investigation of the phenomenon of exchange bias in thin film form requires the selection of a suitable AFM and its successful growth in different crystallographic orientations and heterostructure configurations. We have identified the ordered intermetallic MnPd alloy with a $L1_0$ ordered structure and a tetragonal unit cell (a_0∼0.407 nm, c_0∼0.358 nm) as the appropriate AFM. For MnPd, the spin structure based on bulk measurements [69] is uncompensated (non-zero net spin on the interface plane, and with spin direction normal to the interface) for the (100) surface but compensated (zero net spin on the interface plane, but with spin direction also in plane) for the (001) surface. We have successfully grown a MnPd film epitaxially on MgO (001) single crystals, using an Fe primary layer (t∼60 Å), with both a-axis and c-axis normals [70]. Using alloy targets of similar compositions, we have found that at low substrate temperatures the growth of MnPd is dominated by the kinetics and forms a disordered structure, albeit with the a-axis normal. These films can be annealed to obtain a chemically ordered film with a (100) normal. At higher substrate temperatures, the growth process is thermodynamically driven and forms the stable ordered structure with a c-axis normal. On the other hand, growth of "normal" structures, i.e. MgO|MnPd|Fe can also be accomplished by growing at the higher temperature range. The latter gives the largest exchange bias suggesting the use of texture as a predictive principle for EB.

The growth and structural properties of the epitaxial film with orientation relationship given by $MgO_{(001)}||MnPd_{(001)}||Fe_{(001)}$ and $MgO_{[100]}||MnPd_{[100]}||Fe_{[110]}$ was investigated extensively by X-ray diffraction [71]. X-ray $\theta - 2\theta$ scans showed that the orientation of the MnPd unit cell and the crystalline quality could be controlled as a function of the deposition temperature. Pole figure measurements or texture scans revealed a pure a-axis orientation for films grown below 100°C while single-crystalline c-axis films are obtained above 450°C. Intermediate temperatures yield a mixture of both orientations with a poor crystalline quality. Moreover, based on low angle X-ray reflectivity measurements, it was shown that the interface quality strongly depends on the deposition temperature and also the order in which MnPd and Fe

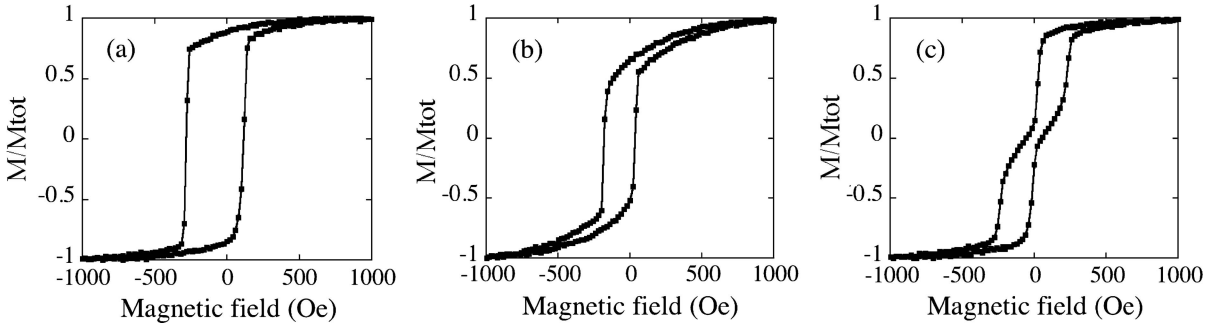

Figure 10 Measured hysteresis loops with the applied field, H, along different crystallographic directions. (a) H applied along Fe [100] (bias direction), (b) H applied along Fe [110] (45 deg to the bias direction) and (c) along the Fe [010] direction (perpendicular to the bias direction).

are deposited. The X-ray reflectivity data (not shown) reveals finite thickness oscillations with two distinct wavelengths: the short wavelength oscillations are due to the total thickness of the film while the longer ones arise from the Fe layer. Fitting the reflectivity data to a Paratt model [72], indicates a MnPd/Fe interface roughness of the order of 2.5 Åfor our highest quality films grown with a substrate temperature above 450°C.

The magnetization process of these high quality, exchange-biased MnPd/Fe bilayers was investigated using vibrating sample and torque magnetometry. The former was measured as a function of in-plane orientation, with respect to the directions of bias and easy axes of magnetization, and three distinct loops were observed (Fig. 10). A simple analytical model [73] based on coherent magnetic moment rotation [74] was used to qualitatively explain and describe the magnetization process. The shift of the hysteresis loop, the increased coercivity, the easy and hard axis behavior as well as the intermediate magnetic state seen in the hysteresis loops are reproduced in the model. However, the magnitude of the bias and the coercivity are not strictly in agreement with the measured values. The discrepancies are attributed to the simplified model which does not take into account the role of magnetic domains or disorder at the MnPd/Fe interface.

The magnetization processes in these exchange-biased MnPd/Fe bilayers were further investigated using polarized neutron reflectivity [75]. The measurements show that by breaking the symmetry of the intrinsic, cubic, four-fold anisotropy of the Fe film the induced unidirectional anisotropy radically changes the magnetization processes. If the exchange bias is large the induced unidirectional anisotropy is able to pull the net magnetization of the sample to the bias direction after saturation along any of the magnetic hard Fe<110> directions. However, if the exchange bias is small it will only give rise to a difference in net magnetization along the magnetic easy axes adjacent to the saturation direction. Thus, the net magnetic moment along the bias direction depends on the relative magnitudes of the cubic and the unidirectional anisotropy. However, both the magnetization and the neutron reflectivity measurements show that the net magnetic moment along the bias direction at zero field is less than the total magnetic moment of the sample (M[100]<1). If the magnetization reversal occurs by coherent magnetic moment rotation, M[100] would be equal to one. This suggests that magnetic domains are formed when the magnetic field is reduced from saturation. However, neither the neutron reflectivity nor the magnetization measurements provide any information on the distribution of the sample magnetization—only the components of the net magnetization is measured—and a suitable imaging technique needs to be employed.

Photoemission electron microscopy (PEEM) was carried out utilizing the PEEM2 X-ray photoemission electron microscope at the Advanced Light Source. In a photoemission electron microscope the sample is irradiated by X-rays of variable polarization and photon energy. The resulting emission of low energy secondary electrons from the surface are then magnified onto a screen by electrostatic lenses and a spatial resolution [76] of typically 50 nm can be achieved. Magnetic contrast of the Fe film is obtained in such a microscope by using circular polarized X-rays and acquiring images at the Fe L_3 (706.8eV) and Fe L_2 (719.9 eV) core level absorption edges (X-ray magnetic circular dichroism or XMCD). Images shown here are the result of a division of these two images. Because the ratio between these two absorption intensities is determined by the projection of the magnetization onto the helicity of the incoming light it allows for the unambiguous identification of the direction of the magnetic moment in a domain. The sample was saturated in a magnetic field of 1500 Oe along a specific crystal axis before the magnetic domain images were taken.

PEEM images from the Fe/MnPd bilayer are shown in Fig. 11. It also shows a grey scale legend that links the direction of the magnetization to the image intensity. Note that the grey color corresponds to both horizontal magnetization directions, since XMCD contrast appears between “up” and “down” but not between “left” and “right” domains. The PEEM image for the *descending* remnant magnetic state after saturation along Fe [110] is

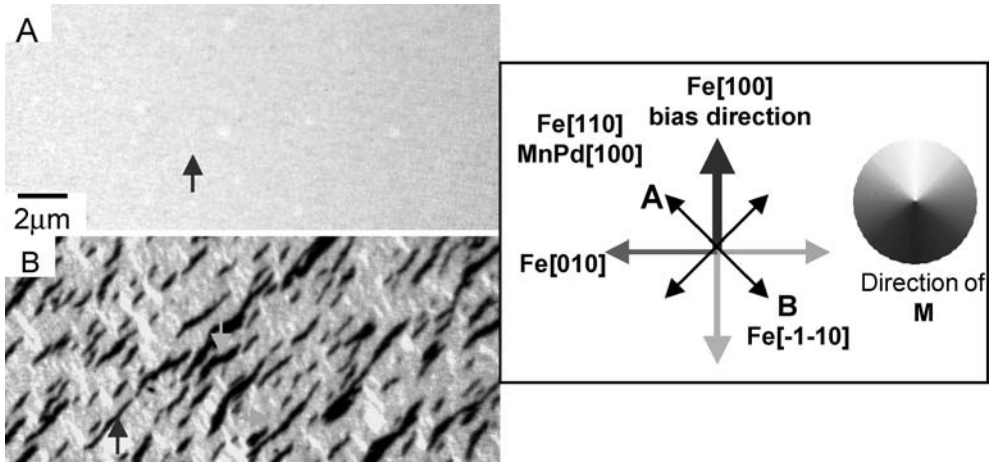

Figure 11 Photoemission electron microscopy images of exchange-biased samples at the remnant state on, (a) the descending and (b) the ascending branch of the hysteresis loops. The various crystallographic orientations and a guide to the direction of magnetization are also shown.

shown in Fig. 11A. No magnetic domains are observed in the image. Thus, the unidirectional anisotropy (or EB) is strong enough to pull the sample magnetization to the bias direction (Fe [100]). For comparison, in an unbiased Fe (001) film the magnetization along the two magnetic easy directions next to Fe [110] is expected to be equal since the probability for the magnetization to rotate clockwise and counterclockwise is the same.

The corresponding PEEM image for the *ascending* remnant magnetic state after saturation along the Fe [-1-10] direction is shown in Fig. 11B. Magnetic domains are in this case clearly visible. The magnetization in the domains is oriented along three of the four in-plane magnetic easy directions: Fe [0-10] (grey), Fe [-100] (black), and Fe [100] (white). As seen, most of the magnetization is along the Fe [0-10] direction, followed by the Fe [-100] and the Fe [100]. The domains with the magnetization along the bias direction (Fe [100]) are due to the induced unidirectional anisotropy; they are not expected in an unbiased Fe (001) film after saturation along Fe [-1-10]. Thus, the magnetization along the bias direction is the reason for the large difference in remnance between the descending and ascending loop. The domains with magnetization parallel and opposite to the bias direction are elongated with a width of $\sim$0.5 μm and a length of $\sim$1–5 μm; moreover, the long axes of these domains are perpendicular to each other with 90° Néel walls oriented along the Fe$\langle$110$\rangle$ directions. This type of domain wall is the most energetically favorable type in ultrathin films with magnetic easy axes oriented 90° with respect to each other. Thus, the magnetization is not along the long axis of the domains, but instead makes an angle of 45° with it. It should be noted that both the elongated shape and the perpendicular orientation of the Fe [-100] and the Fe [100] domains are due to the fact that most of the sample magnetization is along the Fe [0-10] direction. This means for the Fe [-100] domains that only domain walls parallel to the Fe [1-10] (or equivalently Fe [-110]) direction are energetically favorable. Domain walls parallel to Fe [110] (or Fe [-1-10]) give rise to stray fields because the magnetization is not continuous across these walls. Similarly, for the Fe [100] domains the magnetostatic energy is minimized if the domain walls are oriented along the Fe [110] (or Fe [-1-10]) direction.

Magnetic reversal in ferromagnetic materials occurs either by coherent rotation or by domain nucleation. Generally, the mechanism is an intrinsic function of the microstructure and is symmetric with respect to the applied field. In other words, on either branch of the hysteresis loop only one (and the same) of these two mechanisms is observed. Based on these PEEM measurements we have shown, for the first time, direct imaging evidence for the asymmetry in magnetic reversal mechanism in exchange biased systems that is beyond the scope of indirect scattering measurements [77]. This was made possible by detailed X-ray photoemission electron microscopy imaging on carefully prepared samples which had been previously well-characterized magnetically including neutron reflectivity measurements. The magnetization reversal occurs by moment rotation for decreasing fields while it proceeds by domain nucleation and growth for increasing fields. The observed domains are consistent with the crystallography of the bilayers and favor a configuration that minimizes the overall magnetostatic energy of the ferromagnetic layer.

3.2. Exchange bias and perpendicular anisotropy in thin metal films and multilayers

Combining the concepts of perpendicular anisotropy and exchange bias, we have investigated perpendicular ex-

change bias, i.e. the coupling between Co/Pt multilayers with perpendicular anisotropy and antiferromagnetic materials. Such investigations of perpendicular exchange bias would lead to a better understanding of the nature of the interfacial spin structure and magnetic coupling in FM/AFM structures. Initially a variety of critical growth parameters for both the AFM layer and the FM multilayer stacks, including the thicknesses of the Co and Pt layers, seed layer materials, thin film orientations, number of bilayer repeats and substrate temperature, were carefully optimized. As a result, high quality multilayers composed of $Pt_{200\ Å}/(Co_{6\ Å}/Pt_{20\ Å})_5$/FeMn were grown on Si (001) substrates at room temperature by ion-beam sputtering. An external magnetic field of 400 Oe, perpendicular to the thin film plane, was applied during thin film growth using a permanent magnet and a large perpendicular exchange bias was observed.

In such thin film heterostructures, the physical properties are sensitive to the structural parameters such as the crystalline orientation, strain, roughness, and interdiffusion at the interface. In particular, both the FM/AFM and the FM/NM interfaces are very important for perpendicular exchange biased multilayer systems and by varying ion-beam energy, the interdiffusion at the FM/NM and FM/AFM interface can be well-controlled. The samples were structurally characterized by X-ray reflectivity (XRR) and in general, we found that the lower ion-beam energy deposited multilayers have lower interdiffusion at the interface. Fig. 12 shows the XRR scans of $(Co_{6\ Å}/Pt_{20\ Å})_5$ multilayer samples deposited with different ion-beam energy of 250 eV, 500 eV and 750 eV. As the ion-beam energy increases, the multilayers have a more rapid fall off of satellite intensity. The third-order satellite peak can be clearly seen in Fig. 12A but is almost negligible in Fig. 12B and 12C. Associated data fitting using the commercially available Bede REFS (Build 4.00.13) program shows that the densities of the Co layers vary proportionally with ion-beam energy and, in all cases, are significantly higher than the bulk value. This is consistent with the fact that the energy of sputtered elements increases with increasing Ar^+ ion energy leading to a deeper penetration and larger inter-diffusion.

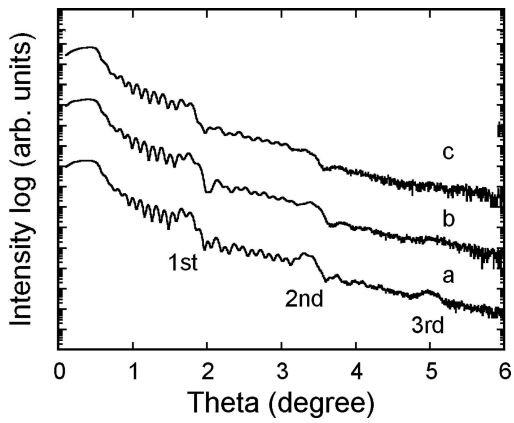

Figure 12 X-ray reflectivity (XRR) of $(Co/Pt)_n$ multilayers grown with different Ar^+ ion-beam energies (a) 250 eV (b) 500 eV (c) 750 eV.

The inter-diffusion effect on perpendicular exchange bias can be investigated by comparing the perpendicular anisotropy energy and exchange-bias field of samples grown with different ion-beam energies. Fig. 13A shows the room temperature, out-of-plane hysteresis loops of the same three $(Co_{6\ Å}/Pt_{20\ Å})_5$ multilayers grown with ion-beam energy from 250 to 750 eV. As ion-beam energy increases, the effective anisotropy constant change from $K_{eff} = 4.17\times10^6$ erg/cm^3 to $K_{eff} = 1.25\times10^6$ erg/cm^3 and $K_{eff} = -3.75\times10^5$ erg/cm^3 for ion-beam energy of 250 eV, 500 eV and 750 eV, respectively. From the magnitude and the change in sign of K_{eff}, it can be seen that the transition from perpendicular anisotropy to in-plane occurs with increasing ion-beam energy.

It is clear that the lower ion-beam energy enhances the perpendicular anisotropy with best results obtained for 250 eV. The ion-beam energy also affects the exchange-bias field. Fig. 13B shows the hysteresis loops of representative multilayers of $(Co_{6\ Å}/Pt_{20\ Å})_5/FeMn_{80\ Å}$. All the $(Co_{6\ Å}/Pt_{20\ Å})_5$ stacks were grown with ion-beam energy of 250 eV, while the FeMn layers were grown with different ion-beam energies varying from 250 to 1500 eV. The ion-beam energy dependence of H_c and H_{eb} is shown in the inset of Fig. 13B. It is noticed that H_{eb} drops rapidly from 135 Oe to 45 Oe when the FeMn layers were grown with higher ion-beam energy. H_c also decreases as the ion-beam energy increases, possibly due to the competition between perpendicular anisotropy induced by the Co/Pt interfaces and the large in-plane anisotropy induced at the terminating Co/FeMn interface together with the overall shape anisotropy of the film.

In conclusion, structural-property correlations have been investigated and it has been found that multilayers deposited with lower ion-beam energy have lower interdiffusion at the interface, and thus have stronger perpendicular magnetic anisotropy and larger exchange bias. Work in progress include theoretical modeling of the effect of interdiffusion on perpendicular exchange bias; extraordinary hall effect (EHE) [78] investigation of Co/Pt and (Co/Pt)/FeMn multilayers to study the sensitivity of electron transport to the magnetic multilayers interfaces and magnetic force microscopy (MFM) investigation of the domain formation and motion during the magnetization reversal process.

3.3. Perpendicular domain formation and transport characteristics of ferromagnetically coupled bilayers

In magnetic thin films, the orientations of the magnetic moments can be perpendicular or parallel to the surface of

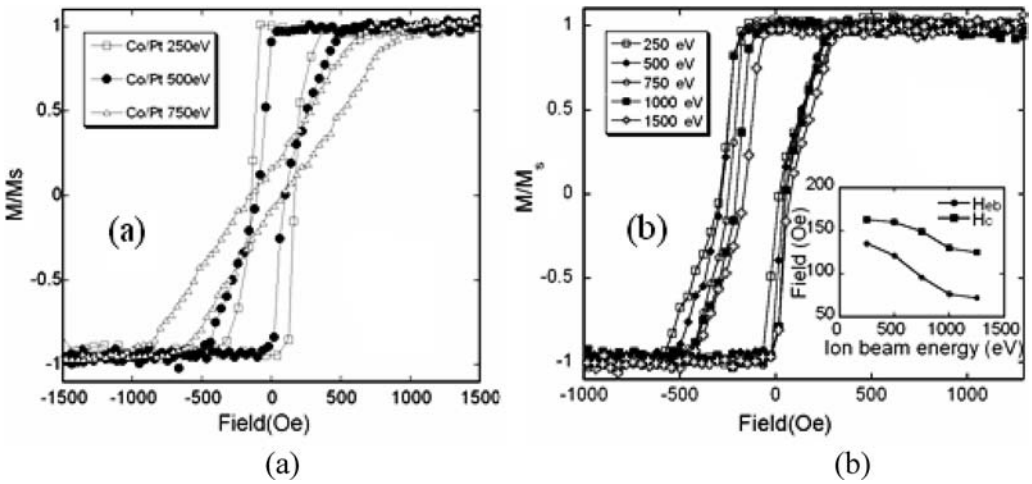

Figure 13 Out-of-plane hysteresis loops of (a) $(Co/Pt)_n$ multilayers without bias grown with different Ar^+ ion-beam energies. (b) $(Co/Pt)_n$/FeMn multilayers in which FeMn was deposited with different ion-beam energies. Inset, exchange bias field (H_{eb}) and coercivity (H_c) versus ion-beam energy.

the system and is commonly called out-of-plane and in-plane, respectively. Most ferromagnetic metal thin films show in-plane domain structures [79] unless their film thickness is less than 1∼2 nm. However, a stripe domain structure [80] with significant out-of-plane character can be achieved in thin film form, when materials such as Yttrium Iron Garnet (YIG) are grown along certain crystallographic direction because of its high perpendicular magnetocrystalline anisotropy. If a ferromagnetic film is then grown on top of such a garnet film exhibiting stripe domains, up to a certain thickness (<20 nm), it is expected to mimic the domain structure of the garnet underlayer. In our investigation, the perpendicular domain coupling between a ferromagnetic metal and the garnet underlayer has been studied in detail. Micromagnetic simulations show that the exchange stiffness energy term, which is the interaction energy between nearest-neighbor atoms at the interface, is the main cause of a perpendicular domain structure in Fe films rather than a long range surface exchange energy term. Finally, work in progress includes measurements of the magnetoresistance including the domain wall resistance due to local spin-dependent electron scattering at the domain wall. In principle, using this system the position of the domain wall in the metallic ferromagnet can be modulated by the underlying stripe domain of the garnet layer but the domain wall-width is determined by the intrinsic properties of the metallic ferromagnet. Since the domain wall of this ferromagnetic metal layer is perpendicular to the current direction, the magnetoresistance due to domain wall scattering can be measured.

3.3.1. Experimental details

In this preliminary experiment, a commercial YIG layer grown by liquid phase epitaxy (LPE) on a gadolinium gallium garnet (GGG) single crystal was used as substrate. To study the domain coupling between ferromagnetic metal and magnetic oxide layers, a series of test samples were prepared using an ion beam sputtering system. A soft ferromagnetic metal Fe was deposited on the YIG/GGG substrate at room temperature. The thickness of Fe, t_{Fe} was varied (0, 5, 10 and 20 nm). Magnetic hysteresis of such thin films were measured (Fig. 14) using the magneto-optic Kerr effect (MOKE) [81]. Depending on the direction of magnetization and the direction of light propagation, both in-plane and out-of-plane hysteresis loops were measured. A square-shaped hysteresis loop for out-of-plane measurements was observed for all t_{Fe}<20 nm. For t_{Fe}=20 nm, the out-of-plane loop shows a linear shape, but the in-plane loop shows a square-shaped hysteresis, indicating that the preferred magnetization direction is in-plane.

Magnetic Force Microscopy (MFM) is a powerful technique to investigate the surface domain structure of magnetic materials. MFM uses a two-pass technique for imaging the domain structure. The first pass measures the topography using contact or tapping mode, and the second pass measures the interaction force between tip and sample using lift mode. Thus, MFM allows a detailed correlation of magnetic and structural features at the surface. Both topography (Atomic Force Microscopy or AFM) and MFM images of the Fe/YIG samples are shown in Fig. 15. In the AFM images, as the thickness of Fe layer is increased the surface of the film appears to be getting smoother. The corresponding MFM images (Fig. 15) reveal a stripe domain structures for t_{Fe} = 5, 10 nm, but not for t_{Fe} = 20 nm. Since the stripe domain images are the characteristics of magnetization structures with significant out-of-plane contribution, these results are in good agreement with the results from the MOKE measurements. Also, the domain patterns of both 5 nm and 10 nm Fe films are very similar to that of the YIG only

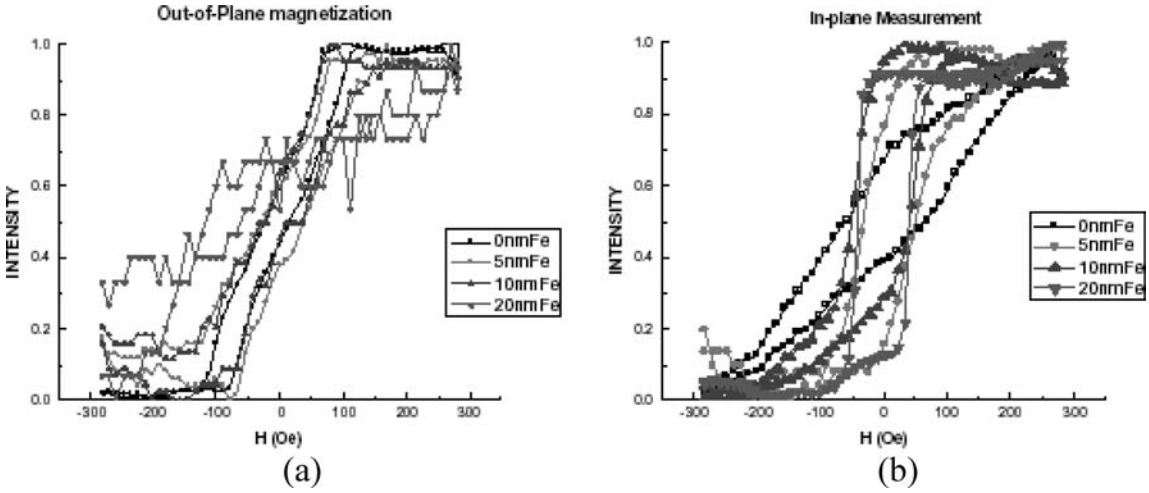

Figure 14 MOKE results of Fe/YIG/GGG sample with Fe thickness of 0 nm, 5 nm, 10 nm, 20 nm. The hysteresis loops are measured for both (a) out-of-plane and (b) in-plane.

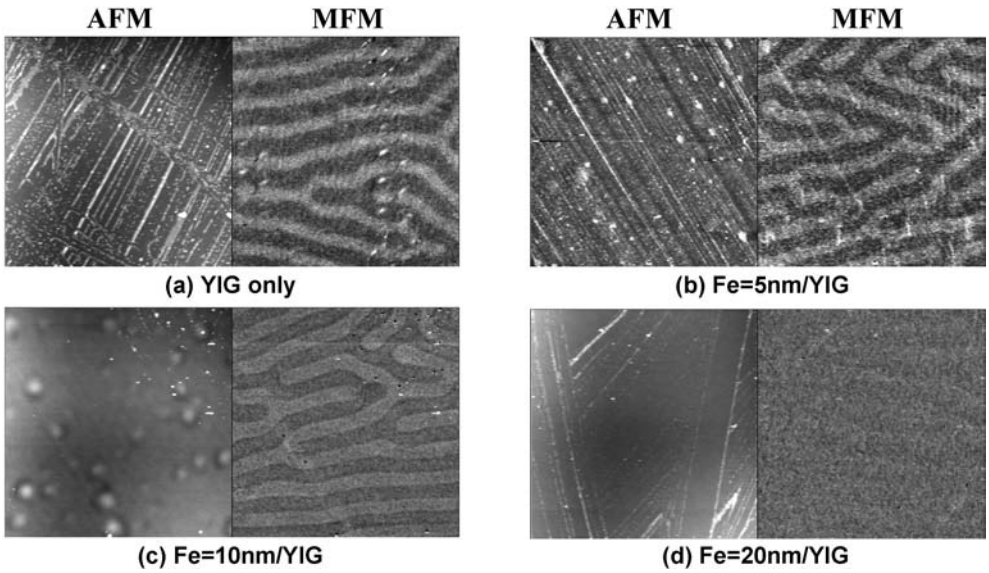

Figure 15 Topography (AFM) and domain structure (MFM) of Fe/YIG/GGG samples with Fe thickness of (a) 0 nm, (b) 5 nm, (c) 10 nm, (d) 20 nm. (Scanning area: 40 μm × 40 μm).

sample in both shape and dimension. This suggests that the domain structure of YIG film is maintained in the Fe film due to the strong magnetic coupling between the layers [82].

3.3.2. Micromagnetic simulation

The experimental results show that the domain configuration observed in Fe/YIG bilayer structures arises from a strong interlayer exchange interaction between the Fe and YIG layers. To verify these results, micromagnetic simulation was performed on Fe 10 nm/YIG double layer configuration using OOMMF (Object Oriented Micromagnetic Framework) [83]. The volume exchange stiffness energy and the interface energy term with both bilinear and biquadratic contributions are the two energy terms, which determine the domain structure of Fe/YIG sample. Bilinear exchange coupling is the interlayer coupling, which leads to antiparallel alignment of the magnetic layers, and biquadratic exchange coupling is the interlayer coupling, which leads to a 90° relative orientation of the magnetization in adjacent magnetic layers. The volume exchange stiffness energy is expressed as [84]:

$$E_{\text{ex}} = A_{\text{interface}} \int (\nabla \cdot m)^2 \text{dV} \qquad (1)$$

where $A_{\text{interface}}$, the exchange stiffness constant (J/m) at the interface. m is the normalized unit spins (i.e. magnetization direction) at each cell. Another energy term, the

interface contribution to the energy density between two thin films can be expressed as [85 , 86]:

$$E_{\text{coupl}} = C_{\text{bl}}\,(1 - m_1 \cdot m_2) + C_{\text{bq}}[1 - (m_1 \cdot m_2)^2] \quad (2)$$

where C_{bl} and C_{bq} are the bilinear and biquadratic surface exchange constants, and m_1 and m_2 are the normalized, unit spins (i.e., magnetization directions) at adjacent cells in two different materials. The Fe/YIG bilayer domain structure was simulated while varying the values of $A_{\text{interface}}$, C_{bl} and C_{bq} and keeping all other materials parameters fixed to their bulk values. For fixed $A_{\text{interface}}$, but with the bilinear and biquadratic surface exchange constants varied over a wide range, from 0 to 1×10^{-4} J/m^2, the simulations always show an in plane domain configuration for the Fe film. On the other hand, a strong interlayer coupling between the Fe and YIG film, which shows the perpendicular domain configuration of the Fe film when the interface exchange stiffness coefficient ($A_{\text{interface}}$) is varied. These simulations show that the observed interlayer coupling between Fe and YIG layers can be attributed to a strong volume exchange stiffness energy contribution.

4. Wide band-gap, doped, magnetic oxides for spintronics applications

The rapidly developing field of spin electronics requires a semiconducting room temperature ferromagnet for incorporation in proposed spin-electronic devices. There are certain materials requirements in order to have a spintronic device. These are: efficient electrical injection of spin-polarized carriers (spin injection) into the semiconductor, sufficient spin diffusion lengths and lifetimes for spin transport through the semiconductor, control and manipulation of the spin signal, and efficient spin detection for determining output [87]. In addition, for any sort of commercial device, room temperature operation is a must. Materials that have the potential to satisfy these requirements are dilute magnetic semiconductors (DMS). A DMS is composed of a nonmagnetic semiconducting matrix with spins of the magnetic (transition metal) dopant ions coupled ferromagnetically, and ideally, providing spin polarized charge carriers for conduction of the signal. In this context, studies of transition-metal doped, wide band-gap materials are of current interest both in the solid-state physics and materials science communities. Our work in this field is both active and varied. Initial work was focused on multilayers comprised of alternating nanoscale layers of a semiconductor and a magnetic metal. This resulted in samples ranging from a superparamagnetic granular material to a DMS multilayer stack. Subsequently, we have progressed to the incorporation of a randomly distributed magnetic dopant within a semiconducting matrix resulting in dilute magnetic dielectrics (DMD) [38].

DMS such as Mn:GaAs have received the most attention as spin injector materials for spintronics [36, 37] because they allow for impedance matching to the semiconductor device, a requirement for efficient injection [35]. The functionality of such devices has been limited thus far by low ferromagnetic ordering temperatures, with T_C~170 K. In the search for materials compatible with room temperature operation, there has been significant focus recently on wide band gap semiconductors such as TiO_2 [88, 89], ZnO [90], GaN [91, 92], GaP [93], AlN [94, 95], and SnO_2 [96, 97] as the host DMS material. The two most prominent issues that limit further development of such transition metal (TM) doped oxides for room temperature spintronics are difficulties that can arise from phase segregation and lack of understanding of the fundamental mechanism associated with their ferromagnetic ordering. Phase segregation of transition metal dopants (which can act as extrinsic sources of ferromagnetism) in the oxide host has to be strictly avoided. Instead, preparation of a homogeneous solid solution of the TM dopant incorporated into the oxide host is necessary to determine if these materials do in fact exhibit intrinsic ferromagnetic behavior. It is important to note that in the case of secondary phase formation of the magnetic dopant atoms, insufficient characterization leads to skewed results, causing much controversy in determining whether these complex material systems can be used as true DMS. Even in the cases where secondary phase formation can be ruled out, there has been a wide range of results for the same material grown and processed under different conditions and in different laboratories, which makes it difficult to propose a comprehensive explanation for their high T_C ferromagnetic behavior. These issues continue to present themselves as an exciting topic in the field of magnetic materials, and much still needs to be investigated both experimentally and theoretically.

4.1. Co doped anatase TiO_2—a dilute magnetic dielectric

With the initial discovery of room temperature ferromagnetism in Co doped anatase TiO_2 [88, 89], this compound has been one of the most prominent of the potential oxide DMS materials [98]. However, due to the observation of Co metal clusters in some cases, there has been much speculation on the origin of ferromagnetism in such TM doped oxides. On the other hand, some recent experiments have also ruled out the presence of clusters, confirmed room temperature ferromagnetism in these materials [92, 93] and correlated the ferromagnetism to n-type semiconducting behavior. Although these results appear promising for Co:TiO_2 as a potential DMS, the true origin of ferromagnetism and whether the carriers are spin-polarized are yet

to be determined. It is hence of vital importance to clarify the correlation (if any) between carriers and the mechanism of ferromagnetism inherent to this structure. Towards this end, thin films of Co-doped anatase were grown by RF magnetron sputter deposition. Because anatase is a metastable phase of TiO_2, films need to be grown at elevated temperatures (550°C) at relatively slow growth rates (0.01 nm/s) and on lattice-matched substrates. Here we present results for films grown on $LaAlO_3$ (100) or LAO. The films were then annealed in ultra high vacuum (UHV) for 1 h at 450°C. Structural, compositional, and magnetic measurements were made on films before and after annealing.

X-ray diffraction (XRD) verified that the as-deposited films were single phase anatase with no evidence of secondary phases within the detection limits of X-ray scattering experiments. The effect of the post-growth annealing treatment in UHV at 450°C for 1 h is shown by the change in the anatase (004) peak from the XRD $\theta-2\theta$ scan in Fig. 16. The FWHM value of the film peak is shown to decrease by -0.20° after annealing, which illustrates the improvement in crystalline quality of the film. Also, it can be seen that the peak position shifts to the right with annealing, indicative of a relaxation of the anatase lattice along the *c*-direction. This is most likely attributable to strain relaxation, diffusion of defects through the lattice (oxygen vacancies) and/or incorporation of Co ions into equilibrium lattice positions. Fig. 17 demonstrates the high quality anatase crystal structure observed in high resolution transmission electron microscopy (HRTEM) images of cross-sectional as-deposited (A) and UHV annealed (B) specimens. The selected area diffraction pattern (inset) reveals single crystal (004) anatase epitaxially grown onto the LAO substrate. EDXS data taken at a number of locations throughout the specimens reveal a solid solution of Co dissolved in anatase, with Co concentrations ranging from ~2–7 at.% incorporated into the lattice. Analysis of energy filtered images using hydrogenic cross-sections also shows a uniform distribution of cobalt with an average concentration of 2.8% Co in the anatase lattice [99]. Rutherford backscattering spectroscopy measurements confirm that the bulk Co composition as a function of film depth is uniform with an average of ~2 at% [100]. Moreover, there was no evidence for the presence of Co metal or Co-rich (above 7 at%) anatase clusters within the films in any of these detailed TEM measurements.

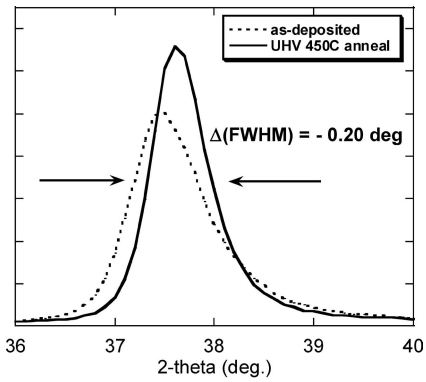

Figure 16 XRD 2θ scan of $Co:TiO_2$ anatase (004) peak before and after annealing.

Near edge X-ray absorption fine structure (NEXAFS) at the Co K-edge were measured on annealed and as-deposited $Co:TiO_2$ films to determine the oxidation state and local geometry of the Co dopant in the lattice. As-deposited and annealed films exhibited nearly identical NEXAFS spectra; for clarity Fig. 18 [38] shows only the annealed sample spectrum compared to the following reference samples: $CoTiO_3$, CoO, and Co metal. The onset of absorption in the NEXAFS spectra of the $Co:TiO_2$ films are a close match to $CoTiO_3$ and CoO, where Co has been interpreted to be in the +2 oxidation state. On the other

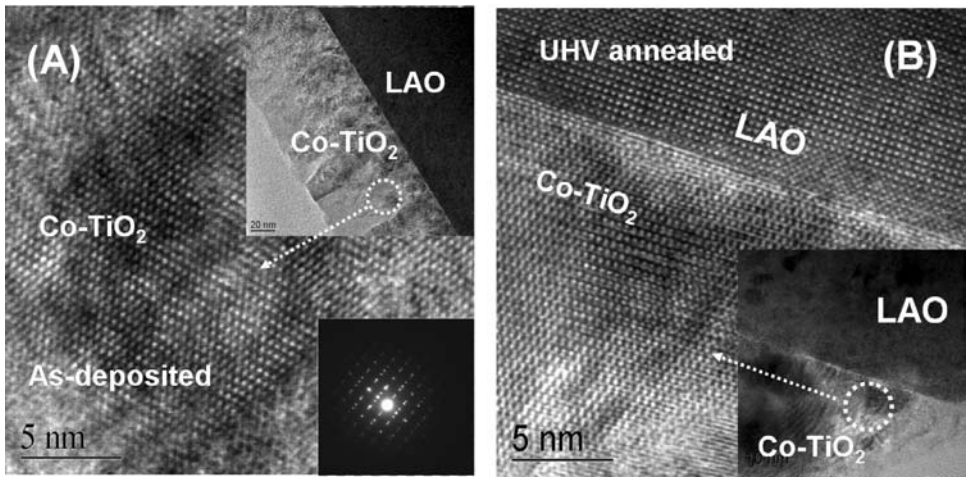

Figure 17 High resolution TEM images from cross-section specimens of as-deposited (A) and UHV annealed (B) $Co:TiO_2$ films on LAO. Insets: Low magnification images, and selected area diffraction pattern.

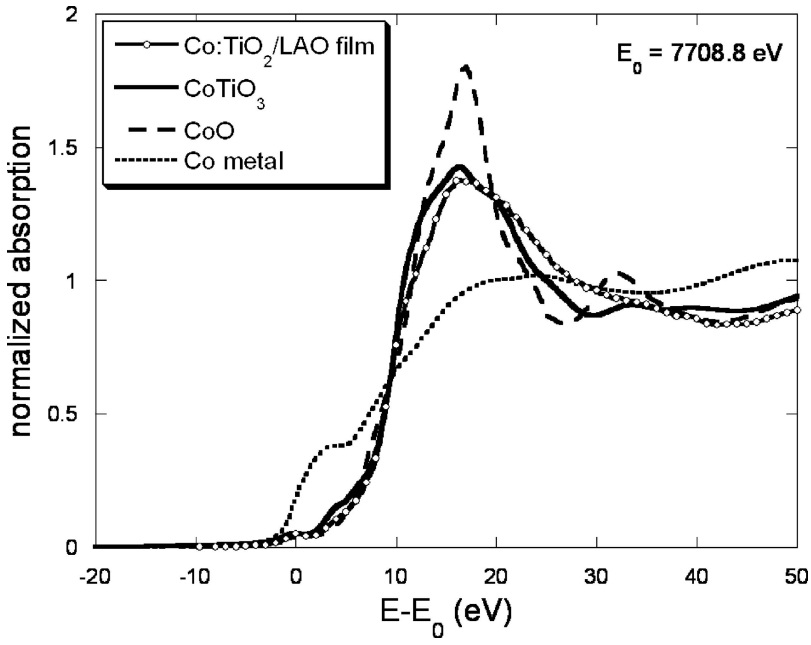

Figure 18 Co K-edge NEXAFS spectra for UHV annealed $Co:TiO_2$ film with reference samples: $Co:TiO_2$ film (open circles), $CoTiO_3$ (solid line), CoO (long dash), and Co metal (short dash) spectra (reproduced from [38]).

hand, the absorption edge of Co metal is a poor match to the $Co:TiO_2$ films due to the much lower threshold energy corresponding to the Co(0) state. The closer match of NEXAFS spectrum of the sputtered $Co:TiO_2$ film to $CoTiO_3$ than to CoO is indicative of the distorted octahedral coordination of the Co atom in the lattice (i.e. Ti site in anatase), whereas in CoO the Co site has an undistorted octahedral configuration. From this comparison of Co K-edge spectra it can be concluded that there is no evidence of Co metal throughout the film and Co^{2+} substitutes for Ti^{4+} in the lattice.

Magnetic hysteresis loops (M vs H) at 300 K of as-deposited and annealed $Co:TiO_2$ films in Fig. 19A show the increase in spontaneous magnetization, M_S, from 0.24 to 1.17 μ_B/Co atom with annealing. The TRM measurements (Fig. 19B) were taken in zero applied field after the sample was saturated, and the remanent magnetization, M_R, as a function of increasing temperature was recorded. (TRM is useful as a direct measurement of the magnetic signal from the $Co:TiO_2$ film alone because the measurement is taken in zero applied field and there is no contribution from the diamagnetic LAO substrate.) The TRM results from 5–365 K demonstrate the enhancement of M_R from 0.07 to 0.34 μ_B/Co atom with annealing. Coercivity, H_C, also increases with annealing, from ~100 to ~300 Oe.

Both as-deposited and annealed samples are all highly insulating and have sheet resistances $\geq 10^{11}$ Ω/square. Thus resistivity is at least greater than 10^6 Ω cm for all samples. The fascinating co-existence of room temperature ferromagnetism in the dielectric state brings to light many questions regarding the possible ferromagnetic exchange mechanisms in TM doped oxides. The XRD experimental results suggest that the improved crystallinity of the films after UHV annealing would be the primary factor for the enhanced ferromagnetism. However, the 450°C annealing process in UHV also provides thermal energy for the creation and diffusion of oxygen vacancies (V_O's) through the lattice. The V_O's created during the annealing that are necessary for the enhanced ferromagnetic properties do not provide free carriers for conduction. Rather, we propose that the carriers associated with creation of V_o's are trapped on Co_{Ti} defect sites [101, 102]. With sufficient thermal energy provided by the annealing treatment, both the V_O migration and trapping is possible, leading to the enhancement of magnetic properties. We therefore attribute the enhanced ferromagnetism to the combination of the increase in crystallinity, the creation/diffusion of defect centers and trapping of carriers with the annealing process.

4.2. Other examples of DMD - Co:ZnO and Cr:ZnO systems

Alternating deposition of atomic-scale layers of ZnO and Co, with aluminum doping, with varying semiconductor and metal thicknesses results in a range of magnetic and electronic properties [104]. A series of multilayer samples were deposited via Ion Beam Sputtering (IBS), ZnO thicknesses ranged from 2–20 Å and Co thicknesses ranged from 2–10 Å with the total number of bilayers varying between 15 and 25. The samples were deposited at constant deposition rates on Si and glass substrates. Additionally, through collaboration, we were able to com-

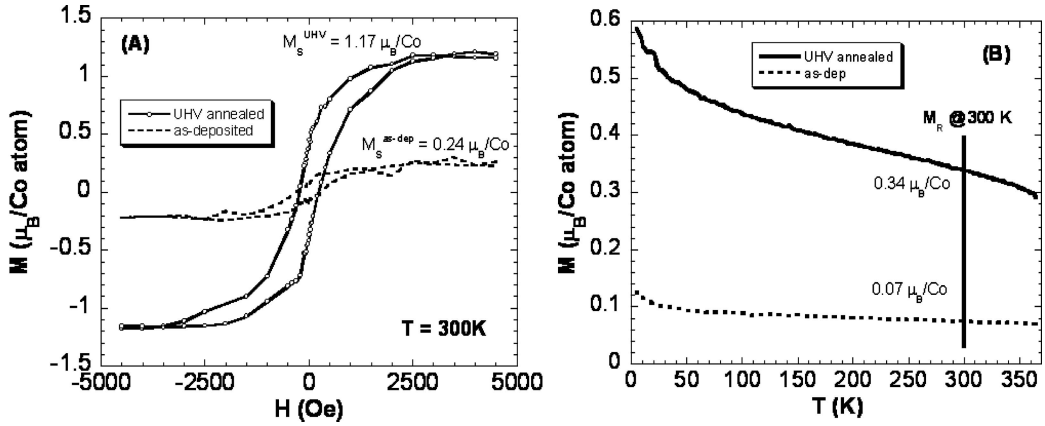

Figure 19 Magnetic measurements from SQUID magnetometer: (A) *M-H* loops at 300 K of as-deposited (dashed line) and UHV annealed (solid line) Co:TiO_2 films. (The diamagnetic contribution from the LAO substrate has been subtracted from the experimental data.) (B) M_R vs. *T* of same films.

pare this multilayer system with equivalent single crystal ZnO:Co samples prepared by the metalorganic chemical vapor deposition (MOCVD) process [105].

RBS studies showed the Co/Zn atomic ratios ranging from 0.1 to 1.25, consistent with the expected values depending on the details of the multilayer stack, an excess of oxygen compared to Zn in stoichiometric ZnO, and about 5% of aluminum (donor dopant). XRD for a $(ZnO_{20\ Å}Co_{2\ Å})_{25}$ sample on a glass substrate reveals the nanocrystalline structure of ZnO, primarily *c*-axis oriented, and exhibiting no peaks of metallic Co. Samples with larger relative Co content indicated diffuse metallic Co reflections. Zero field-cooled and field-cooled magnetization measurements were made as a function of temperature in a field of 20 Oe (Fig. 20) for samples with fixed nominal thickness of 2 Å of Co layers and varying (2–20 Å) ZnO thickness with magnetization normalized to the nominal total volume of Co. Higher relative content of Co results in a granular multilayer structure, which demonstrates magnetic blocking phenomena and superparamagnetism. Blocking is seen from splitting of the zero field cooled (ZFC) and field cooled (FC) curves, and, for the sample with the thinnest ZnO layers, $(ZnO_{2\ Å}Co_{2\ Å})_{25}$, a maximum in the ZFC susceptibility near the blocking temperature. The sample with the thickest ZnO layers, $(ZnO_{20\ Å}Co_{2\ Å})_{25}$, behaves as a diluted magnetic semiconductor, i.e. it does not show any sign of blocking phenomena down to 2.5 K, and its magnetization does not go to zero at high *T*, and remains approximately constant in the temperature range 40–300 K. M vs H dependences for this sample are hysteretic both at 10 K and 300 K. Loops with no hysteresis typical of superparamagnetic materials are observed above the blocking temperature in samples with small relative ZnO thickness (2–10 Å) to Co (2 Å). The transition from granular 2D to magnetic semiconductor 3D material is further evidenced by the following transport measurements.

Resistivity of granular samples with high relative Co concentrations follows a variable range hopping (VRH)

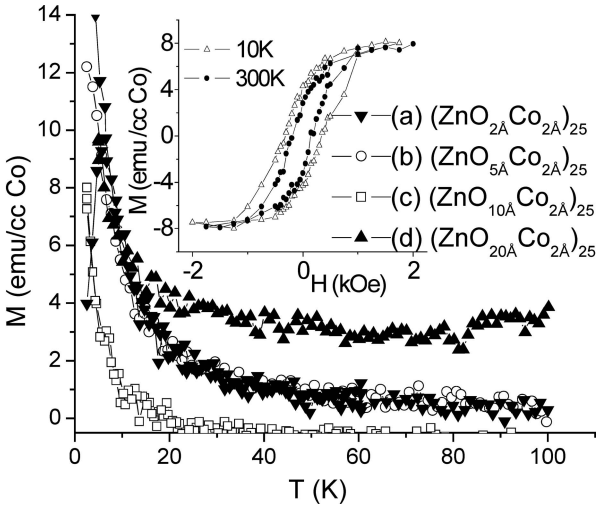

Figure 20 ZFC and FC magnetization measurements at H=20 Oe for samples with varying nominal thickness of ZnO layers x $(ZnO_{x\ Å}Co_{2\ Å})_{25}$, normalized to the total nominal volume of Co metal. Inset: Magnetic hysteresis loops measured on sample $(ZnO_{20\ Å}Co_{2\ Å})_{25}$ at 10 K and 300 K.

law (ln $\rho \sim (T_0/T)^n$+constant) with *n* close to 1/2, typical of hopping between metal granules in an insulator at intermediate temperatures [105] evidenced in Fig. 21. We've also shown [104] that a crossover from the dominating quasi-2D ($n \gtrsim 1/2$) to 3D ($n \lesssim 1/2$) variable range hopping occurs as the ZnO nominal thickness increases. Upon further increase of ZnO thickness, with $n \sim 1$, the ferromagnetic sample $(ZnO_{20\ Å}Co_{2\ Å})_{25}$ behaves like that of an Al doped ZnO film with no Co doping.

There are two competing channels of conduction in the system, which differ in the temperature dependence of resistivity. Increasing the total relative amount of Co in the films, at a fixed Al doping level, increases the resistivity of the semiconductor. Hence, cobalt impurities, while necessary for the presence of magnetic moments, provide traps for carriers which mediate magnetic order. With further decreasing ZnO layer thickness, the number of Co metal

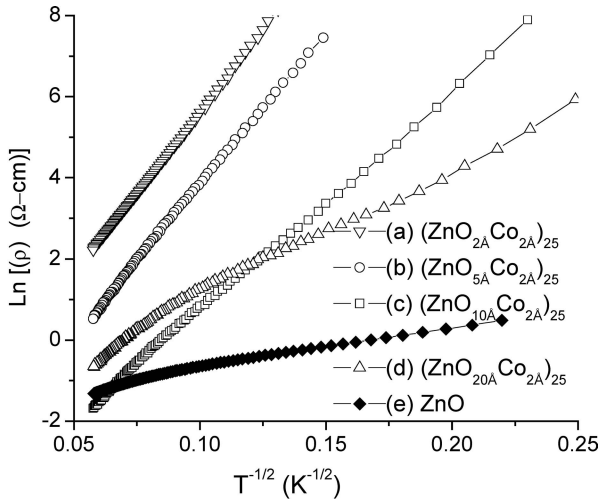

Figure 21 Logarithm of resistivity as a function of $1/T^{1/2}$.

inclusions grows, which leads to increasing conductivity via inter-granular tunneling (hopping) channel. The ferromagnetic sample $(ZnO_{20\ Å}Co_{2\ Å})_{25}$ contains no metal inclusions, based on both magnetic and structural results. We assume that, due to limited diffusion length at a given ambient deposition conditions, the semiconductor superlattice consists of cobalt-rich, low carrier-concentration layers, alternating with layers lightly doped with Co, and hence having higher carrier concentration. Though conducting due to Al doping, neither ZnO:Co bulk films grown by MOCVD, or the superlattice films already covered, show an appreciable anomalous Hall contribution. Additionally, magnetically doped ZnO DMS films show qualitatively similar magnetoresistance to undoped films [104]. This suggests that the ferromagnetism in DMS films is not carrier mediated, indicating that a different ferromagnetic exchange mechanism is at play.

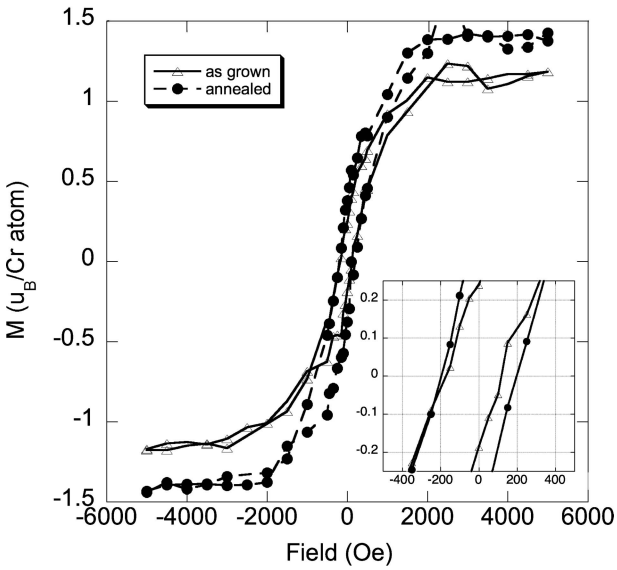

Figure 22 Hysteresis loops of as grown and annealed samples showing increase in M_s, M_R. The inset shows the coercive fields.

Magnetic doping of wide gap semiconductors including ZnO and TiO_2 bearing no relationship to the presence of free carriers has resulted in a new class of spintronic materials tentatively titled dilute magnetic dielectrics (DMD) as discussed above. As an additional proof of this concept, thin films of ZnO doped with Cr grown via magnetron co-sputtering have resulted in magnetic dielectric films [106]. Grown on a-plane sapphire, *c*-axis oriented polycrystalline ZnO films with Cr concentration of roughly 9.5 at.% show a per-ion saturation moment of 1.4 μ_B. The films show open *M-H* plots (Fig. 22) and remanent magnetization at temperatures exceeding 365 K. The lack of conductivity excludes the possibility of carrier-mediated ferromagnetism, and structural characterization (XRD) does not indicate the existence of any secondary phases (to contribute to the ferromagnetism in these films, a secondary phase would have to make up a significant volume fraction of the film).

5. Concluding remarks

Research in the area of magnetism and magnetic materials has undergone a tremendous transformation during the last couple of decades. It is a rich combination of new theoretical concepts, synthesis, measurement and characterization techniques, where both the materials structure and "device" engineering is carried out at the nanometer length scales. Magnetic materials are also central to new applications ranging broadly from information storage, biology and medicine to new principles of electronics and even quantum computing. In addition to traditional studies of magnetic soft/hard materials, current scientific interest is also focused on magnetic quantum dots, superlattices, precision doping and magneto-electronics. Hence, many quantum phenomena more familiar to semiconductor physics also play a vital role in these magnetic studies. This also means that the whole area of magnetism is becoming more synthetic, multidisciplinary and intellectually demanding. In this brief overview of our recent work we have demonstrated broadly this blend of materials synthesis, microstructure, new physics and novel applications. However, the format of this article does not allow the discussion of some other interesting work being carried out in our laboratory. This includes, for example, studies of materials for magnetic actuations in microelectromechanical systems (MEMS) applications, and spin-resolved quantum conductance in nanoscale break junctions. Details of these projects and our broad research program can be found on our website [107].

Acknowledgements

Our research program at the University of Washington was supported by the following grants: NSF/DMR #0203069,

NSF/DMR #0322729, NSF/ECS #0224138, DoE/BES #DE-FG03-02ER45987, NSF/DMR #0315460. KMK also acknowledges the Campbell endowment at UW for their continued support. Graduate students involved in this research were also supported by the UW-PNNL JIN fellowship (KG, YB) and the NPSC/ARCS/Boeing Engineering Scholarship (MG). We thank all our collaborators for their help and support

References

1. G. HADJIPANAYIS (ed.), Magnetic Recording Beyond 2000, (Kluwer Academic Press, 2001).
2. L. M. FALICOV, D. T. PIERCE, S. D. BADER, R. GRONSKY, K. B. HATHAWAY, H. J. HOPSTER, D. N. LAMBETH, S. S. P. PARKIN, G. PRINZ, M. SALAMON, I. K. SCHULLER and R. H. VICTORA, *J. Mater. Res.* **5** (1990) 1299.
3. F. J. HIMPSEL, J. E. ORTEGA, G. J. MANKEY and R. F. WILLIS, *Adv. Phys.* **47** (1998) 511.
4. H. KRONMULLER in Modern Problems in Metal Physics II" edited by A. Seeger (Springer, Berlin, 1966).
5. C. KITTEL, *Rev. Mod. Phys.* **21** (1949) 541.
6. E. H. FREI, S. SHTRIKMAN and D. TREVES, *Phys Rev.* **106** (1957) 446.
7. C. P. BEAN, *J. Appl. Phys.* **26** (1955) 1381.
8. G. HERTZER, *IEEE Trans. Mag.* **25** (1989) 3327.
9. J. M. D. COEY (ed.), Rare-Earth Iron Permanent Magnets (Oxford, 1996).
10. D. C. CREW, ER. GIRT, M. GUILOT, D. SUESS, T. SCHREFL and K. M. KRISHNAN, *Phys. Rev.* **B66** (2002) 184418.
11. E. GIRT, K. M. KRISHNAN and G. THOMAS, *Scripta Materialia* **44** (2001) 1431.
12. G. J. KUSINSKI, K. M. KRISHNAN, G. DENBEAUX, G. THOMAS, B. D. TERRIS and D. WELLER, *Appl. Phys. Lett.* **79** (2001) 2211.
13. V. K. LA MER and R. H. DINEGAR, *J. Amer. Chem. Soc.* **72** (1950) 4847.
14. L. BRUS, *J. Phys. Chem. Solids* **59** (1998) 459.
15. H. J. G. DRAAISMA, W. J. M. DE JONGHE and F. J. A. DEN BROEDER, *J. Mag. Mag. Mater.* **66** (1987) 351.
16. J. NOGUES and I. K. SCHULLER, *ibid.* **192** (1999) 203.
17. E. F. KNELLER and R. HAWIG, *IEEE Trans. Mag.* **27** (1991) 3588.
18. J. B. KORTRIGHT, D. D. AWSHALOM, J. STOHR, S. D. BADER, Y. U. IDZERDA, S. S. P. PARKIN, I. K. SCHULLER and H. C. SIEGMAN, *J. Mag. Mag. Mat.* **20** (1999) 7.
19. K. M. KRISHNAN, in NATO/ASI on Magnetic Recording Beyond 2000, edited by G. Hadjipanayis (Kluwer Academic Press, 2001) p. 251.
20. A. MORRISH, The Physical Principles of Magnetism (Wiley, NY, 1965).
21. C. LEIGHTON, J. NOGUES, B. J. JÖNSSON-ÅKERMAN and IVAN K. SCHULLER, *Phys. Rev. Lett.* **84** (2000) 3466.
22. U. WELP, S. G. E. TE VELTHUIS, G. P. FELCHER, T. GREDIG and E. D. DAHLBERG, *J. App. Phys.* **93** (2003) 7726; S. G. E. TE VELTHUIS, A. BERGER, G. P. FELCHER, B. K. HILL and E. DAN DAHLBERG, *ibid.* **87** (2000) 5046.
23. Y. IJIRI, J. A. BORCHERS, R. W. ERWIN, S. H. LEE, P. J. VAN DER ZAAG and R. M. WOLF, *Phys. Rev. Lett.* **80** (1998) 608.
24. P. BLOMQVIST, KANNAN M. KRISHNAN and ER. GIRT, *J. Appl. Phys.* **95** (2004) 8487; C. LEIGHTON, M. R. FITZSIMMONS, P. YASHAR, A. HOFFMAN, J. NOGUES, J. DURA, C. F. MAJKRZAK and IVAN K. SCHULLER, *Phys. Rev. Lett.* **86** (2001) 4394.
25. M. R. FITZSIMMONS, P. YASHAR, C. LEIGHTON, IVAN K. SCHULLER, J. NOGUES, C. F. MAJKRZAK and J. A. DURA, *ibid.* **84** (2000) 3986; M. GIERLINGS, M. J. PRANDOLINI, H. FRITZSCHE, M. GRUYTERS, D. RIEGEL, *Phys. Rev.* **B65**, (2002) 092407; V. I. NIKITENKO, V. S. GORNAKOV, A. J. SHAPIRO, R. D. SHULL, K. LIU, S. M. ZHOU and C. L. CHIEN, *Phys. Rev. Lett.* **84** (2000) 765; V. I. NIKITENKO, V. S. GORNAKOV, L. M. DEDUKH, YU.P. KABANOV, A. F. KHAPIKOV, A. J. SHAPIRO, R. D. SHULL, A. CHAIKEN and R. P. MICHEL, *Phys. Rev.* **B57** (1998) R8111.
26. A. P. MALOZEMOFF, *Phys. Rev.* **B37** (1988) 7673; N. C. KOON, *Phys. Rev. Lett.* **78** (1997) 4865; T. C. SCHULTHESS and W. H. BUTLER, *ibid.* **81** (1998) 4516; R. L. STAMPS, *J. Phys. D: Appl. Phys.* **33** (2000) R247.
27. P. BLOMQVIST, KANNAN M. KRISHNAN, H. OHLDAG, A. SCHOLL and J. STÖHR, *Phys. Rev. Lett.* **94** (2005) 107203.
28. L. NEEL, *J. Phys. Radium* **15** (1954) 225.
29. N.-H. CHO, KANNAN M. KRISHNAN, C. LUCAS and R. F. C. FARROW, *J. Appl. Phys.* **72** (1992) 5799.
30. M. ZIESE and M. J. THORNTON (eds.), "Spin Electronics" (Springer-Verlag, Berlin, Heidelberg, New York, 2001).
31. M. N. BAIBICH, J. M. BROTO, A. FERT, F. N. VANDAU, F. PETROFF, P. EITENNE, G. CREUZET, A. FRIEDERICH and J. CHAZELAS, *Phys. Rev. Lett.* **61** (1988) 2472.
32. V. S. SPERIOSU, B. DIENY, P. HUMBERT, B. A. GURNEY and H. LEFAKIS, *Phys. Rev.* **B44** (1991) 5358.
33. J. S. MOODERA, L. R. KINDER, T. M. WONG and R. MESERVEY, *Phys. Rev. Lett.* **74** (1995) 3273.
34. P. NAJI, M. DURLAM, S. TEHRANI, J. CALDER and M. DEHERRERA, 2001 IEEE International Solid State Circuits Conference, (2001) p. 437.
35. G. SCHMIDT and L. W. MOLENKAMP, *Physica E* **10** (2001) 484.
36. Y. OHNO, D. K. YOUNG, B. BESCHOTEN, F. MATSUKURA, H. OHNO and D. D. AWSCHALOM, *Nature (London)* **402** (1999) 790.
37. S. A. WOLF, D. D. AWSCHALOM, R. A. BUHRMAN, J. M. DAUGHTON, S. VON MOLNAR, M. L. ROUKES, A. Y. TCHELKANOVA and D. M. TREGER, *Science* **294** (2001) 1488.
38. K. A. GRIFFIN, A. B. PAKHOMOV, C. M. WANG, S. M. HEALD and KANNAN M. KRISHNAN, *Phys. Rev. Lett.* **94** (2005) 157204.
39. L. REIMER, "Transmission Electron Microscopy" (Springer-Verlag, 1997).
40. M. VARELA, W. GROGGER, D. ARIAS, Z. SEFRIOUI, C. LEON, C. BALLESTEROS, KANNAN M. KRISHNAN and J. SANTAMARIA, *Phys. Rev. Lett.* **86** (2001) 5156.
41. J. SANTAMARIA, M. E. GOMEZ, J. L. VICENT, KANNAN M. KRISHNAN and I. SCHULLER, *ibid. 89* (2002) 190601.
42. N. CHENG, KANNAN M. KRISHNAN, ER. GIRT, R. F. C. FARROW, R. MARKS, A. YOUNG and H. A. CHENG, *J. Appl. Phys.* **87** (2000) 6647.
43. G. DENBEAUX, P. FISCHER, G. KUSINSKI, M. LE GROS, A. PEARSON and D. ATTWOOD, *IEEE Trans. Magn.* **37** (2001) 2764.
44. A. SCHOLL, H. OHLDAG, F. NOLTING, J. STÖHR and H. A. PADMORE, *Rev. Sci. Instrum.* **73** (2002) 1362.

45. P. TARTAJ, *Encycl. Nanosc. Nanotech.* **6** (2004) 823.
46. V. F. PUNTES, KANNAN M. KRISHNAN and P. A. ALIVISATOS, *Science* **291** (2001) 2115.
47. Y. BAO, A. B. PAKHOMOV and K. M. KRISHNAN, *J. Appl. Phys.* **97** (2000) 10J317.
48. V. K. LAMER and R. H. DINEGAR, *J. Am. Chem. Soc.* **72** (1950) 4847.
49. Y. BAO, M. BEERMAN, A. B. PAKHOMOV and K. M. KRISHNAN, *J. Phys. Chem. B.* **109** (2005) 7220.
50. Y. BAO, M. BEERMAN and K. M. KRISHNAN, *J. Mag. Mag. Mat.* **266** (2003) L245.
51. T. C. LUBENSKY, *Solid State Commun.* **102** (1997) 187.
52. W. ZHOU, A. KUMBHAR, J. WIEMANN, J. FANG, E. E. CARPENTAR and C. J. O'CONNER, *J. Solid State Chem.* **159** (2001) 26.
53. S-J. CHO, S. M. KAUZLARICH, J. OLAMIT, K. LIU, F. GRANDJEAN, L. REBBOULH and G. J. LONG, *J. Appl. Phys.* **95** (2004) 6804.
54. J. L. LYON, D. A. FLEMING, M. B. STONE, P. SCHIFFER and M. E. WILLIAMS, *Nanoletters* **4** (2004) 719.
55. A. K. GUPTA and M. GUPTA, *Biomaterials* **26** (2005) 3995.
56. Y. BAO and K. M. KRISHNAN, *J. Magn. Magn. Mater.* **293** (2005) 15.
57. S. MORNET, S. VASSEUR, F. GRASSET and E. DUGUET, *J. Mater. Chem.* **14** (2004) 2161.
58. J. C. RIFE, M. M. MILLER, P. E. SHEEHAN, C. R. TAMANAHA, M. TONDRA and L. J. WHITMAN, *Sens. Actuators A, Phys.* **A107** (2003) 209.
59. L. EJSING, M. F. HANSEN, A. K. MENON, H. A. FERREIRA, D. L. GRAHAM and P. P. FREITAS, *Appl. Phys. Lett.* **84** (2004) 4729.
60. A. B. PAKHOMOV, Y. BAO and K. M. KRISHNAN, *J. Appl. Phys.* **97** (2005) 10Q305.
61. J. CONNOLLY and T. G. ST. PIERRE, *J. Magn. Magn. Mater.* **225** (2001) 156.
62. A. JORDAN, in Scientific and Clinical Applications of Magnetic Carriers, edited by U. Häfeli (Plenum Press, New York, 1997).
63. R. HERGT and W. ANDRA, *IEEE Trans. Magn. (USA)* **34** (1998) 3745.
64. M. GONZALES and K. M. KRISHNAN, *J. Magn. Magn. Mater.* **293** (2005) 265.
65. I. A. BREZOVICH, *Med. Phys. Monograph* **16** (1988) 82.
66. R. E. ROSENSWEIG, *J. Magn. Magn. Mater.* **252** (2002) 370.
67. P. C. FANNIN, B. K. P. SCAIFE and S. W. CHARLES, *ibid.* **72** (1988) 95.
68. J. A. C. BLAND and B. HEINRICH (eds), "Ultrathin Magnetic Structures I & II" (Springer-Verlag, 1994).
69. L. PAL, K. KREN, G. KADAR, P. SZABO and T. TARNOCZI, *J. Appl. Phys.* **39** (1968) 538.
70. N. CHENG, J. P. AHN and KANNAN M. KRISHNAN, *ibid.* **89** (2001) 6597.
71. P. BLOMQVIST, KANNAN M. KRISHNAN and D. E. MCCREADY, *ibid.* **95** (2004) 8019.
72. L. G. PARRAT, *Phys. Rev.* **95** (1954) 359.
73. P. BLOMQVIST and KANNAN M. KRISHNAN, *J. Appl. Phys.* **95** (2004) 8487.
74. E. C. STONER and E. P. WOHLFARTH, *Proc. Phys. Soc.* **A240** (1948) 599.
75. P. BLOMQVIST, KANNAN M. KRISHNAN, S. SRINATH and S. G. E. TE VELTHUIS, *J. Appl. Phys.* **96** (2004) 6523.
76. A. SCHOLL, H. OHLDAG, F. NOLTING, J. STÖHR, H. A. PADMORE, *Rev. Sci. Instrum.* **73** (2002) 1362.
77. P. BLOMQVIST, KANNAN M. KRISHNAN and H. OHLDAG, *Phys. Rev. Lett.* **94** (2005) 107203.
78. C. L. CANEDY, X. W. LI and G. XIAO, *J. Appl, Phys.* **81** (1997) 5367.
79. A. BERGER and H. HOPSTER, *Phys. Rev. Lett.* **76** (1996) 519.
80. C. KOOY and U. ENZ, *Philips Research Reports* **15** (1950) 7.
81. J. P. QIAN and G. C. WANG, *J. Vac. Sci. Technol.* **A8** (1990) 4117.
82. Y. S. CHUN and KANNAN M. KRISHNAN, *J. Appl. Phys.* **95** (2004) 6858.
83. M. J. DONAHUE and D. G. PORTER, Interagency Report NISTIR 6376, OOMMF User's Guide, Version 1.0. (1999).
84. L. D. LANDAU and E. LIFSHITZ, *Physik. Z. Sowjet Union* **8** (1935) 153.
85. J. SLONCZEWSKI, *J. Magn. Magn. Mat.* **150** (1995) 13.
86. A. ROSENCWAIG, W. J. TABOR and R. D. PIERCE, *Phys. Rev. Lett.* **26** (1971) 779.
87. B. T. JONKER, S. C. ERWIN, A. PETROU and A. G. PETUKHOV, *MRS Bulletin* **28** (2003) 740.
88. Y. MATSUMOTO, M. MURAKAMI, T. SHONO, T. HASEGAWA, T. FUKUMURA, M. KAWASAKI, P. AHMET, T. CHIKYOW, S.-Y. KOSHIHARA and H. KOINUMA, *Science* **291** (2001) 854.
89. S. A. CHAMBERS, S. THEVUTHASAN, R. F. C. FARROW, R. F. MARKS, J. U. THIELE, L. FOLKS, M. G. SAMANT, A. J. KELLOCK, N. RUZYCKI, D. L. EDERER and U. DIEBOLD, *Appl. Phys. Lett.* **79** (2001) 3467.
90. K. UEDA, H. TABATA and T. KAWAI, *ibid.* **79** (2001) 988.
91. S. KUWABARA, T. KONDO, T. CHIKYOW, P. AHMET and H. MUNEKATA, *Jpn. J. Appl. Phys. Part 2* **40** (2001) L724.
92. M. K. REED, N. A. EL-MASRY, H. H. STADELMAIER, M. K. RITUMS, M. J. REED, C. A. PARKER, J. C. ROBERTS and S. M. BEDAIR, *Appl. Phys. Lett.* **79** (2001) 3473.
93. N. THEODOROPOULOU, A. F. HEBARD, M. E. OVERBERG, C. R. ABERNATHY, S. J. PEARTON, S. N. G. CHU and R. G. WILSON, *Phys. Rev. Lett.* **89** (2002) 107203.
94. S. G. YANG, A. B. PAKHOMOV, S. T. HUNG and C. Y. WONG, *Appl. Phys. Lett.* **81** (2002) 2418.
95. Y. WU, H. X. LIU, L. GU, R. K. SINGH, L. BUDD, M. VAN SCHILFGAARDE, M. R. MCCARTNEY, D. J. SMITH and N. NEWMAN, *ibid.* **82**, (2003) 3047.
96. S. B. OGALE, R. J. CHOUDHARY, J. P. BUBAN, S. E. LOFLAND, S. R. SHINDE, S. N. KALE, V. N. KULKARNI, J. HIGGINS, C. LANCI, J. R. SIMPSON, N. D. BROWNING, S. DAS SARMA, H. D. DREW, R. L. GREENE and T. VENKATESAN, *Phys. Rev. Lett.* **91** (2003) 077205.
97. J. M. D. COEY, A. P. DOUVALIS, C. B. FITZGERALD and M. VENKATESAN, *Appl. Phys. Lett.* **84** (2004) 1332.
98. S. R. SHINDE *et al.*, *Phys. Rev.* **B67** (2003) 115211; J.-Y. KIM, J. H. PARK, B. G. PARK, H. J. NOH, S. J. OH, J. S. YANG, S. D. BU, T. W. NOH, H. J. LIN, H. H. HSIEH and C. T. CHEN, *Phys. Rev. Lett.* **90** (2003) 017401; S. A. CHAMBERS ET AL., *Thin Sol. Films* **418** (2002) 197; S. A. CHAMBERS, S. M. HEALD and T. DROUBAY, *Phys. Rev.* **B67** (R) (2003) 100401; S. A. CHAMBERS and R. F. C. FARROW, *MRS Bulletin* **28** (2003) 729; G. C. HAN *et al.*, *J. Magn. Magn. Mater.* **268** (2004) 159.
99. M. VARELA, K. A. GRIFFIN, S. PENNYCOOK and KANNAN M. KRISHNAN (unpublished).
100. RBS measurements courtesy of V. Shutthanandan, Pacific Northwest National Laboratory, Richland, WA.
101. M. S. PARK, S. K. KWON and B. I. MIN, *Phys. Rev.* **B65** (2002) 161201R.
102. K. A. GRIFFIN, A. B. PAKHOMOV, C. M. WANG, S. M. HEALD and KANNAN M. KRISHNAN, *J. Appl. Phys.* **97** (2005) 10D320 (Note: Undoped TiO2 prepared and annealed under the same conditions is conducting.)
103. A. B. PAKHOMOV, B. K. ROBERTS and K. M. KRISH-

NAN, *Appl. Phys. Lett.* **83** (2003) 4357.
104. A. B. PAKHOMOV, B. K. ROBERTS, V. SHUTTHANANDAN, D. MCCREADY, S. T. THEVUTHASAN, A. TUAN, S. A. CHAMBERS and K. M. KRISHNAN, *J. Appl. Phys.* **95** (2004) 7393.
105. P. SHENG, *Philososphical Magazine* **B65** (1992) 357.
106. B. K. ROBERTS, A. B. PAKHOMOV, V. S. SHUTTHANANDAN and KANNAN M. KRISHNAN, *J. Appl. Phys.* **97** (2005) 10D310.
107. See http://depts.washington.edu/kkgroup for further details.